Investigation of hydraulic fracture branching in porous media with a hybrid finite element and peridynamic approach

Yanan Sun[a], Bin Chen[b], Michael G Edwards[a], and Chenfeng Li *[a,c]

[a]Zienkiewicz Centre for Computational Engineering, College of Engineering,
Swansea University Bay Campus, Swansea SA1 8EN, United Kingdom
[b]Lawrence Berkeley National Laboratory, Berkeley, CA 94720, United States
[c]Energy Safety Research Institute, College of Engineering, Swansea University Bay
Campus, Swansea SA1 8EN, United Kingdom

Abstract

Simulation of complex fracture patterns in porous media can help understand and improve hydraulic fracturing processes, with potential for significant impact on enhancing oil and gas recovery. In this paper, a fully coupled hydraulic fracture propagation simulation method employing a hybrid finite element method (FEM) and peridynamic (PD) approach is presented. Considering the ability of PD in solving discontinuous problems, the area where cracks can potentially occur is discretised by PD and the crack-free area is discretised by FEM. The solid deformation and fracture propagation are captured by PD and FEM, while the fluid flow in both the reservoir and fracture is simulated with FEM. The whole process is solved in a monolithic way with an implicit scheme. The presented method demonstrates the capability of modelling complex dynamic crack propagation via benchmark examples. Branching phenomenon is then investigated with the proposed model. It is found that faster loading rate, lower-energy release rate, and more brittle and impermeable media will cause crack branching more easily.

Keywords**:** hydraulic fracturing, crack branching, porous media, finite element method, peridynamics, numerical simulation

1 Introduction

Hydraulic fracturing describes the process of injecting fluid with proppant into the wellbore, creating pressure that causes cracks in the rock to develop and spread [1, 5]. It is widely used in the petroleum industry for the development of oil and gas reservoirs, especially low permeability tight formations. In the past few decades, extensive laboratory experiments [7, 27, 28, 33, 75] and field studies [3, 4, 35, 40] have been conducted to study hydraulic fracturing in order to obtain a better understanding of fracture propagation mechanism. In addition, numerical methods are necessary to reveal the fluid-driven fracture behaviors since they are usually more flexible, cheaper and faster to perform compared to laboratory and field experiments. The simulation of hydraulic fracturing in porous media includes three physical processes: (i) deformation of the porous formation, (ii) fluid flow in porous media

---

*Corresponding author: c.f.li@swansea.ac.uk and in the fracture, and (iii) fracture propagation [62]. These processes reveal a strong coupling between the solid formation and the fluid, making the associated numerical simulation a challenging task. Using a numerical approach, this study focuses on the branching of fluid-driven fractures in porous media, which often occurs during hydraulic fracturing and critically affects the productivity enhancement.

Complicated by the occurrence of complex fracture patterns and fluid networks, numerical studies of hydraulic fracturing and branching in porous media are limited. Guo et al. [32] studied hydraulic fracture branching with a phase-field model and concluded that the crack branch occurs when the crack propagates towards stiff rock under certain conditions (e.g. Young's modulus ratio exceeding a critical value) and low in-situ stress difference promotes crack branching. Phase-field models were also developed by Zhou et al. [80], Ni et al. [49] to investigate hydraulic fracture propagation in porous media. It is found in [80] that the final crack branching pattern is not sensitive to the flux rate, and no secondary branches are observed by increasing the flux rate. The influence of energy release rate on hydraulic branching is also studied in [80], where smaller critical energy release rate is found to promote more complex crack branching patterns. The permeability is found to have a limited effect on crack propagation directions [49]. Using a finite element crack band model, Rahimi-Aghdam et al. [56] studied the branching of hydraulic fracture and found the porosity, seepage force (highly related with the permeability), and weak layers are essential for the crack branching phenomenon. Using a bonded-particle model, Zhang et al. [79] investigated fracture patterns in tight sandstone. Complex crack patterns are found more prone to develop under low differential in-situ stress, while the injection of high flow rate and low viscosity fluid are found to encourage dominant fracture development. Ni et al. [52] presented a hybrid finite element and peridynamic model to simulate hydraulic crack branching and found secondary crack branching can occur under higher flux rate. There appears to be a consensus from these limited studies that high injection flow rate leads to crack branching and more complex crack patterns [49, 52, 61, 80]. However, different researchers often come to different conclusions when using different methods, and the effect of various physical parameters on crack branching still needs further investigation.

Commonly used methods for the simulation of fluid-driven fractures include the finite element method (FEM), the extended finite element method (XFEM), the phase-field method (PFM), the discrete element method (DEM) and the peridynamic method (PD). It is noted that each numerical method has its advantages and disadvantages, and a good numerical method should have the ability to simulate complex fracture propagation processes with reasonable computational cost [37]. The aforementioned simulation methods can be roughly classified into two groups: continuum-based and discontinuum-based methods, which are briefly recapped below to put the present study in perspective.

The continuum-based methods for hydraulic fracturing simulation include FEM, XFEM and PFM. The FEM has been successfully applied in hydraulic fracturing simulation for several decades. Boone and Ingraffea [10] presented an early work to simulate hydraulic fracturing using a fully-coupled 2D FEM model. More recently, many other more advanced 2D and 3D FEM models [14, 15, 16, 48, 64] have been developed to simulate hydraulic fracturing in impermeable or porous media, including the use of cohesive zone models to overcome the numerical difficulty caused by stress concentration at fracture tips. To date, the FEM is often used for simple crack geometries (most often horizontal cracks), while for complex crack patterns, e.g. crack branching and multiple branches with time-varying fluid flow network, it becomes almost impossible to achieve a stable and affordable FEM simulation due to the requirement of constant remeshing. Compared with FEM, XFEM avoids/reduces the need of constant mesh updating in the simulation of crack propagation and it has also been applied to hydraulic fracturing problems [59, 44]. However, the requirement of adaptive discontinuous displacement enrichment prevents such XFEM from being applicable to problems in which multiple cracks grow and intersect in complex patterns [39]. Compared with FEM and XFEM, the PFM has advantages in coping with complex fracture patterns since it treats fracture propagation and formation deformation simultaneously as an energy minimization problem, avoiding the tracking of individual fractures and the extra criteria for fracture branching and intersection [17]. The first phase field model to simulate hydraulic fracturing in impermeable materials is developed by Bourdin et al. [11]. Later, the model was expanded for fluid-saturated poroelastic materials by adding poroelastic terms in the energy functional [42, 43] or by utilizing minimization principles for coupling Darcy–Biot-type flow in poroelastic media [41]. However, extremely fine mesh are generally needed in phase field simulation of fracture propagation [17], which sharply increases the computational cost. The discontinuum-based methods include mainly DEM. In DEM [22], the material medium is treated as an assembly of distinct particles and the motion of particles are governed by Newton's laws, thus the discontinuities are the natural outcome of the deformation process. Application of DEM to simulation of hydraulic fracturing is described in [23]. The influence of different parameters including the rock properties, in-situ stress, injection flow rate, fluid viscosity on hydraulic fracturing are also studied with DEM models [46, 78, 26].

Introduced by Silling [66], the peridynamics (PD) is a continuum theory based on integro differential equations, which is a promising tool for studying fracture propagation problems. It uses spatial integrals equations instead of partial differential equations as the controlling equation so as to overcome the limitations of ill-posed partial derivatives at discontinuities, e.g. crack surfaces. In addition, crack growth can be initialised spontaneously with only one simple criterion so that no external criterion is required for complex crack patterns. With advantages in solving discontinuous problems, PD has been widely used for fracture branching analysis [2, 8, 9, 18, 34], which mostly focus on the branching phenomenon in impermeable media. The first application of PD in hydraulic fracturing was reported in [72], in which a new formulation for incorporating the effects of pore pressure is presented to simulate the deformation of porous media. Following this work, Ouchi et al. [55] proposed a hydraulic fracturing model which couples a new PD formulation of porous fluid flow with the existing PD solid formulation together to simulate fluid driven fractures in an arbitrary heterogeneous poroelastic medium. Using a linear viscoelastic PD model, Nadimi et al. [45] simulated hydraulic fracturing initiation and propagation in a 3D heterogeneous geological medium. The simulation work is done by using the PDLAMMPS (peridynamic large-scale atomic/molecular massively parallel simulator) open source software; and the interaction between induced fractures and a pre-existing fracture, as well as the influence of the angle of approach and differential horizontal stress on the fracture propagation behaviour are investigated. Oterkus et al. [54] presented a new fully coupled poroelastic PD formulation by using the analogy between poroelasticity and thermo-elasticity. Combining both advantages of FEM and PD, Ni et al. [52, 53] proposed a hybrid modelling approach for simulating hydraulic fracture in porous media with hybrid FEM and peridynamics to study the hydraulic fracturing behaviour, where a staggered solver is employed. The fluid equation is solved by an implicit time integration iteration while the solid equation is solved by an adaptive dynamic relaxation algorithm, which makes the whole system unconditionally stable.

In this study, we focus on the influence of different parameters on hydraulic fracturing branching in porous media and to balance between efficiency and accuracy, a fully coupled hybrid FEM-PD modelling approach is adopted. Specifically, the solid deformation and fracture propagation are solved by FEM and PD, while the fluid flow equation is solved by FEM. For the solid simulation, the areas where cracks are likely to occur are discretised by PD, and the areas without cracks are discretised by FEM. The Newmark method is employed for time discretisation and the nonlinear system is solved by the Newton-Raphson method. After verification via benchmark examples, a series of computational tests are performed to study the effects of different parameters on hydraulic fracture branching in porous media, providing some useful insights on crack branching mechanisms in porous media.

The rest of the paper is organised as follows. First, § 2 describes the mathematical models and governing equations for hydraulic fracturing. Next, the corresponding numerical solution strategy including space discretisation, time discretisation, coupling strategy, and a simulation flowchart are explained in detail in § 3. Then, in § 4, benchmarks including a one dimensional poroelastic column model [24], a Khristianovic-Geertsma-de Klerk (KGD) model [30, 36] and a crack intersection model are used for verification. Finally, § 5 is devoted to the study of dynamic branching phenomena in porous media, after which conclusions are presented in § 6.

2 Mathematical models for hydraulic fracturing

Hydraulic fracturing is a physically complex procedure where underground rocks are fractured by injecting a viscous fluid [1]. The injected fluid increases the pressure on the surface of the fracture, so as to reach the critical propagation conditions for the crack and split the rock at the crack tip. The fluid driven process includes a strong coupling between the rock deformation, fluid transport in porous media, fluid flow in fractures, and fracture propagation.

2.1 Deformation of a porous formation

In this work, the solid deformation equation is solved by FEM coupled with peridynamics. The FEM is based on classical continuum mechanics, which assumes that a material point only interacts with its immediate neighbors (locality) and the local medium remains continuous as it deforms. The classical FEM formulation is established on spatial derivatives that are undefined at discontinuities. This leads to its limitation in solving discontinuous problems, such as crack propagation problems. Peridynamics is a non-local theory, employing spatial integral equations instead of partial differential equations, see § 2.1.2, which makes it suitable for crack simulation. However, a limitation of the non-local PD theory is the difficulty to accurately represent boundary conditions, see § 3.3 for more details. Recognizing the strength and weakness of FEM and PD, we introduce a hybrid approach to describe continuum deformation.

2.1.1 Classical continuum mechanics description

The deformation of a porous formation is typically modelled by the theory of poroelasticity. The basic theory of poroelasticity was first introduced by Biot [6] (known as the Biot's theory), which was further developed from a physics perspective [60]. For a fully saturated porous medium with a single-phase fluid, the equilibrium equation is

$$\nabla\cdot \boldsymbol{\sigma} + \rho \mathbf{g} - \rho \ddot{\mathbf{u}} = 0 \tag{1}$$

where $\boldsymbol{\sigma}$ is the Cauchy stress, $\mathbf{g}$ is the gravity acceleration, $\ddot{\mathbf{u}}$ is the acceleration of the solid phase, and ρ is the density of the porous medium defined as

$$\rho = (1-n)\rho_s + n\rho_w \tag{2}$$

where n is the porosity, ρ_s and ρ_w are the intrinsic densities of the solid and the fluid, respectively.

The relationship between total stress tensor σ_{ij} and the effective stress tensor σ'_{ij} can be expressed as [70]:

$$\sigma_{ij} = \sigma'_{ij} - I_{ij}\alpha p \tag{3}$$

where p is the pressure of pore fluid, I_{ij} is the identity tensor, and $\alpha = 1 - K_t/K_s$ is the Biot coefficient, with K_t denoting the bulk modulus of the porous skeleton and K_s the bulk modulus of the solid. Biot's coefficient α denotes the ratio of the fluid volume gained (or lost) in a material element to the volume change of that element, and is unity for incompressible solids. The effective stress $\boldsymbol{\sigma}'$ can be determined as:

$$\boldsymbol{\sigma}' = \mathbf{C} : \boldsymbol{\varepsilon}' \tag{4}$$

where $\mathbf{C}$ denotes the elasticity tensor and $\boldsymbol{\varepsilon}'$ the strain tensor.

2.1.2 Peridynamics theory

In the PD theory, a continuum material is treated as a composition of material points $\mathbf{x}$ that interact with other material points $\mathbf{x}'$ inside a horizon $H_{\mathbf{x}}$, and the interactions vanish outside of the horizon, see Fig. 1. The set of points inside the horizon of point $\mathbf{x}$ are denoted as

$$H_{\mathbf{x}} = \mathbf{x}' \in \Omega, |\mathbf{x}' - \mathbf{x}| < \delta \tag{5}$$

where δ is the horizon size (radius of the horizon).

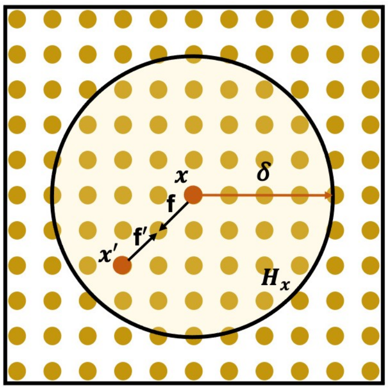

Fig. 1. Interaction of a material point with its neighbouring points.

At a reference position of $\mathbf{x}$ and time t, the peridynamic equation of motion are described by an integral formulation [66]:

$$\rho(\mathbf{x})\ddot{\mathbf{u}}(\mathbf{x}, t) = \int_{H_{\mathbf{x}}} \mathbf{f}(\mathbf{x}' - \mathbf{x}, \mathbf{u}' - \mathbf{u}) dV_{\mathbf{x}'} + \mathbf{b}(\mathbf{x}, t) \tag{6}$$

where ρ is the mass density, $\mathbf{u}$ the displacement vector, $\ddot{\mathbf{u}}$ the acceleration, $\mathbf{b}$ a prescribed body-force density vector, $dV_{\mathbf{x}'}$ the differential volume of $\mathbf{x}'$, $\mathbf{f}$ the force vector between two material points $\mathbf{x}'$ and $\mathbf{x}$. The interaction $\mathbf{f}$ between material points is related to the deformation, pressure and constitutive properties of the material and is called a bond. Crack formations are naturally treated by breaking of bonds. Consequently the spatial integral equations make the PD formulation very attractive for solving discontinuous problems [66]. There are two types of theoretical models for PD: the bond-based PD and the state-based PD. The bond-based PD assumes that any pair of particles interacts only through a central potential that is totally independent of all other local conditions [39]. This assumption results in that for an isotropic, linear, microelastic material, the Poisson's ratio is limited to $1/4$ (plane strain) or $1/3$ (plane stress). To remove the restrictions for Poisson's ratio, the state-based PD was proposed [68], where the interaction between two material points depends not only on the bond between the two points, but also on the deformation of all the other bonds in the horizon. Here, the bond-based PD is intentionally chosen for simplicity with lower computing times with respect to the state-based PD [25].

Based on the bond-based PD theory, the governing equation for solid deformation Eq. (1) is formulated as [54]:

$$\rho(\mathbf{x})\ddot{\mathbf{u}}(\mathbf{x}, t) = \int_{H_{\mathbf{x}}} \lambda c(s - \alpha\gamma\bar{P}) \frac{\boldsymbol{\xi} + \boldsymbol{\eta}}{|\boldsymbol{\xi} + \boldsymbol{\eta}|} dV_{\mathbf{x}'} + \mathbf{b}(\mathbf{x}, t) \tag{7}$$

where $\boldsymbol{\xi} = \mathbf{x}' - \mathbf{x}$ denotes the initial relative position, $\boldsymbol{\eta} = \mathbf{u}' - \mathbf{u}$ the current relative displacement, λ a scalar describing the bond state (i.e. broken or not), c the bond stiffness, γ the coefficient of fluid pore pressure, $\bar{P} = \frac{P(\mathbf{x}',t)+P(\mathbf{x},t)}{2}$ the average fluid pore pressure of points $\mathbf{x}'$ and $\mathbf{x}$, and $s = \frac{|\boldsymbol{\eta}+\boldsymbol{\xi}|-|\boldsymbol{\xi}|}{|\boldsymbol{\xi}|}$ the stretch between material points (i.e. the relative elongation of bond). The fracture propagation is determined by λ and associated failure criteria, for which further details are given in § 2.3. Hydraulic fracturing problems in 2D usually involve the plane strain condition, where the Poisson's ratio is limited to $1/4$. For isotropic materials, c is expressed as:

$$c = \frac{2E}{A\delta^2} \qquad (1D) \tag{8a}$$

$$c = \begin{cases} \frac{6E}{\pi h \delta^3 (1-\nu)} & (2D, \text{plane stress}) \\ \frac{6E}{\pi h \delta^3 (1+\nu)(1-2\nu)} & (2D, \text{plane strain}) \end{cases} \tag{8b}$$

where E is the Young's modulus of the solid skeleton, ν the Poisson's ratio, A the cross-sectional area, and h the thickness. The coefficient of fluid pore pressure γ is defined as:

$$\gamma = \frac{1}{E} \qquad (1D) \tag{9a}$$

$$\gamma = \begin{cases} \frac{1-\nu}{E} & (2D, \text{plane stress}) \\ \frac{(1+\nu)(1-2\nu)}{E} & (2D, \text{plane strain}) \end{cases} \tag{9b}$$

2.2 Fluid flow in porous media and in the fracture

The continuity equation for fluid flow in porous media is

$$\frac{\partial \zeta}{\partial t} + \nabla \cdot \mathbf{q} = 0 \tag{10}$$

where ζ is the variation of fluid volume per unit volume of the porous material, and $\mathbf{q}$ denotes the flux. The flux $\mathbf{q}$ is determined by Darcy's law as:

$$\mathbf{q} = -\frac{\mathbf{k_w}}{\mu} \cdot \nabla p \tag{11}$$

where μ is the fluid viscosity, and $\mathbf{k_w}$ is the permeability tensor. In two dimensions, $\mathbf{k_w}$ is written as:

$$\mathbf{k_w} = \begin{bmatrix} k_x & 0 \\ 0 & k_y \end{bmatrix} \tag{12}$$

where k_x and k_y are principle permeability coefficients in the x and y directions, respectively. The constitutive equation for the pore fluid is

$$p = Q(\zeta - \alpha \varepsilon_b) \tag{13}$$

where Q is the Biot's modulus, α the Biot coefficient, and ε_b the bulk volumetric strain.

The above equations can be combined by substitution and elimination as

$$\alpha \nabla \cdot \dot{\mathbf{u}} + \frac{1}{Q}\dot{p} + \nabla \cdot \mathbf{q} = 0 \tag{14}$$

where $\dot{\mathbf{u}}$ denotes the velocity of the solid phase and $\frac{1}{Q}$ the compressibility coefficient. The first term can be seen as a source term driving pressure distribution and the flux. The compressibility coefficient $\frac{1}{Q}$ is defined as:

$$\frac{1}{Q} = \frac{\alpha - n}{K_s} + \frac{n}{K_w} \tag{15}$$

where K_s and K_w are the bulk module of the solid and fluid phases, respectively.

Note here for a fracture domain, in Eq. (14), the first term of the equation can be neglected. Following the description in [52], the fracture domain is defined as the damage parameter $\phi \geq 0.35$. The permeability k_x and k_y become:

$$\begin{cases} k_x = k_f sin\theta \\ k_y = k_f cos\theta \end{cases} \tag{16}$$

where θ is the direction angle of maximum principal strain. Since the FE mesh has the same grid spacing as PD, the strain is calculated in the FEM context. k_f is the fracture permeability defined as:

$$k_f = \frac{1}{\eta}\frac{w^2}{12} \tag{17}$$

where w is the fracture width calculated via the stretch of the bond [52], and η is a fracture parameter set equal to unity in this study.

2.3 Failure criterion

Compared with FEM, the PD approach treats fracture growth more conveniently and it does not require external criteria for crack propagation direction or crack branching angles. One of the most common criteria in PD is the “critical bond stretch” criterion [67]. When the stretch of the bond s is greater than the critical value s_c, the bond is assumed to be broken, and the pairwise force between the pair of nodes disappears. A history-dependent scalar λ is introduced to describe the bond state: broken or not, such that $\lambda = 1$ when the bond is not broken, $\lambda = 0$ otherwise:

$$\lambda(\mathbf{x}, t, \boldsymbol{\xi}) = \begin{cases} 0 & (s \geq s_c) \\ 1 & (s < s_c) \end{cases} \tag{18}$$

The critical stretch s_c is determined by the critical energy release rate G_c. The relationship between s_c and G_c is defined as [39, 50, 76]:

$$s_c = \begin{cases} \sqrt{\frac{4\pi G_c}{9E\delta}} & (2D, \text{plane stress}) \\ \sqrt{\frac{5\pi G_c}{12E\delta}} & (2D, \text{plane strain}) \end{cases} \tag{19}$$

Note that the break of the bond cannot be recovered. When a series of bonds break, the discontinuous space formed by these broken bonds becomes a macroscopic crack. An example of broken bonds is given in Fig. 2, where a horizon size $\delta = 2\Delta x$ is adopted.

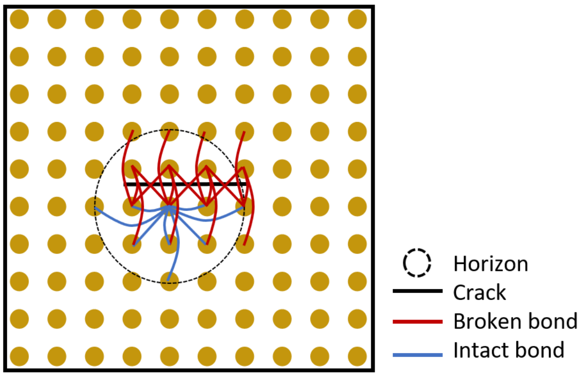

Fig. 2. Crack formed by broken bonds ($\delta = 2\Delta x$).

To describe the crack path, a scalar ϕ called the damage parameter is used. It represents the local damage of point $\mathbf{x}$, which is expressed by the ratio of the sum of the volumes bound to the family nodes connected by the broken bonds to the sum of the volumes of all the family nodes in the original horizon:

$$\phi(\mathbf{x}, t) = 1 - \frac{\int_H \lambda(\mathbf{x}, \mathbf{x}', t) dV_{\mathbf{x}'}}{\int_H dV_{\mathbf{x}'}} \quad 0 \le \phi \le 1 \tag{20}$$

Thus, the value of the damage parameter is between 0 and 1, with 0 representing no failure at the point **x** while 1 representing total failure because all the bonds connected to the point are broken. The crack path can be indicated by plotting the damage parameter.

3 Numerical solution strategy

To solve the mathematical models described in § 2, the numerical simulation needs to deal with two sets of equations, for the solid and the fluid, respectively. As the main focus of this study is the branching phenomenon that involves complex fracture pattern and fluid network, the accuracy, efficiency and robustness are all important for the numerical solution strategy.

As critically reviewed in § 1, peridynamic formulation does not involve spatial derivatives and crack growth is initialised spontaneously without complex propagation criteria, and as such it is advantageous for modelling discontinuous crack propagation problems. In contrast, the FEM is more suitable to describe continuum-based problems with the highest accuracy, i.e. the fluid flow and the porous media deformation without fractures. Based on these observations, a hybrid FEM-PD solution strategy is adopted in this study. Specifically, the solid domain is discretised with FEM and PD dependent on the potential of fracture occurrence, and the fluid domain is discretised with FEM. In this section, the FEM and PD discretisation strategies are explained in § 3.1 and § 3.2, respectively. Then, the coupling strategy and time integration scheme are explained in § 3.3 and § 3.4, respectively. Finally, the simulation workflow is discussed in § 3.5.

3.1 FEM space discretisation of the governing equations

A detailed explanation of the discretisation procedure for the poroelasticity problem with FEM can be found in [81]. The weak form of the governing equations (solid deformation equation Eq. (1) and fluid flow equation Eq. (14)) is first obtained and then the unknown field parameters (the displacement and pressure) are represented by nodal values and interpolation functions. Following the standard FEM discretisation, the discretised governing equations Eq. (1) and equation Eq. (14) can be expressed in a compact matrix form as [10]:

$$\mathbf{M}_F \ddot{\mathbf{u}} + \mathbf{K}_F \mathbf{u} - \mathbf{Q}_F \mathbf{p} = \mathbf{f}_F \tag{21a}$$

$$\mathbf{Q}_F^T \dot{\mathbf{u}} + \mathbf{C}_F \dot{\mathbf{p}} + \mathbf{H}_F \mathbf{p} = \mathbf{q}_F \tag{21b}$$

where **u** denotes the nodal displacement, **p** the nodal fluid pressure, $\mathbf{f}_F$ the nodal force, $\mathbf{q}_F$ the nodal flow source. The coefficient matrices/vectors $\mathbf{M}_F$, $\mathbf{K}_F$, $\mathbf{Q}_F$, $\mathbf{C}_F$ and $\mathbf{H}$ are given by the following expressions:

$$\begin{aligned}
\mathbf{M}_F &= \int_\Omega \mathbf{N}_u{}^T \rho \mathbf{N}_u d\Omega, \ \mathbf{K}_F = \int_\Omega \mathbf{B}_u{}^T \mathbf{D} \mathbf{B}_u d\Omega \\
\mathbf{Q}_F &= \int_\Omega \alpha \mathbf{B}_u{}^T \mathbf{m} \mathbf{N}_p d\Omega, \ \mathbf{m} = \{1, 1, 0\}^T \\
\mathbf{C}_F &= \int_\Omega \frac{1}{Q} \mathbf{N}_p{}^T \mathbf{N}_p d\Omega, \ \mathbf{H}_F = \int_\Omega \mathbf{B}_p{}^T \frac{\mathbf{k}_w}{\mu} \mathbf{B}_p d\Omega
\end{aligned} \tag{22}$$

where $\mathbf{N}_u$ denotes the shape function matrix for displacement, $\mathbf{N}_p$ the shape function matrix for pressure, $\mathbf{B}_u$ the strain-displacement matrix, and $\mathbf{B}_p$ the matrix of first derivatives of the shape functions $\mathbf{N}_p$. Detailed definitions for 2D elements are given in Appendix A.2.

3.2 Peridynamics spatial discretisation of the governing equations

Following the meshless PD discretisation [39], Eq. (7) can be written as:

$$\rho\ddot{\mathbf{u}}_{(i)} = \sum_{j=1}^{N_{(j)}} \lambda c(s_{(i)(j)} - \alpha\gamma\bar{P}_{(i)(j)}) \frac{\boldsymbol{\xi}_{(i)(j)} + \boldsymbol{\eta}_{(i)(j)}}{|\boldsymbol{\xi}_{(i)(j)} + \boldsymbol{\eta}_{(i)(j)}|} V_{(j)} + \mathbf{b}_{(i)} \tag{23}$$

where i and j represent the material points, and $N_{(j)}$ represents the number of material points inside the horizon of point i. Multiplying Eq. (23) by $V_{(i)}$, the volume of material point i, the following equation is obtained:

$$m\ddot{\mathbf{u}}_{(i)} = \sum_{j=1}^{N_{(j)}} \lambda c(s_{(i)(j)} - \alpha\gamma\bar{P}_{(i)(j)}) \frac{\boldsymbol{\xi}_{(i)(j)} + \boldsymbol{\eta}_{(i)(j)}}{|\boldsymbol{\xi}_{(i)(j)} + \boldsymbol{\eta}_{(i)(j)}|} V_{(j)} V_{(i)} + \mathbf{b}_{(i)} V_{(i)} \tag{24}$$

Under the assumption of small deformation, the peridynamics space discretisation for the solid deformation Eq. (24) is expressed as:

$$\mathbf{M}_{PD}\ddot{\mathbf{u}} + \mathbf{K}_{PD}\mathbf{u} - \mathbf{Q}_{PD}\mathbf{p} = \mathbf{f}_{PD} \tag{25}$$

$$\begin{aligned} \mathbf{M}_{PD} &= \mathcal{A}_{i=1}^{N} \rho V_{(i)} \\ \mathbf{f}_{PD} &= \mathcal{A}_{i=1}^{N} \mathbf{b}_{(i)} V_{(i)} \\ \mathbf{K}_{PD} &= \mathcal{A}_{b=1}^{N_{bond}} \mathbf{K}_b \\ \mathbf{Q}_{PD} &= \mathcal{A}_{b=1}^{N_{bond}} \mathbf{Q}_b \end{aligned} \tag{26}$$

where $\mathcal{A}$ is the operator for assembling matrix, $\mathbf{M}_{PD}$ the global mass matrix, $\mathbf{K}_{PD}$ the global stiffness matrix, $\mathbf{f}_{PD}$ the external force, N the number of material points for the whole system, N_{bond} the number of bonds, $\mathbf{K}_b$ the stiffness matrix of the bond between nodes $\mathbf{x}_i$ and $\mathbf{x}_j$, and $\mathbf{Q}_b$ the coefficient matrix for pressure. In the 2D case, the stiffness matrix of the bond $\mathbf{K}_b$ and $\mathbf{Q}_b$ can be described as:

$$\mathbf{K}_b = -\frac{\lambda c V_{(i)} V_{(j)}}{|\boldsymbol{\xi}|} \begin{bmatrix} -cos^2\theta & -cos\theta sin\theta & cos^2\theta & cos\theta sin\theta \\ -cos\theta sin\theta & -sin^2\theta & cos\theta sin\theta & \sin^2\theta \\ cos^2\theta & cos\theta sin\theta & -cos^2\theta & -cos\theta sin\theta \\ cos\theta sin\theta & sin^2\theta & -cos\theta sin\theta & -\sin^2\theta \end{bmatrix} \tag{27}$$

$$\mathbf{Q}_b = -\frac{\lambda c\alpha\gamma V_{(i)} V_{(j)}}{2} \begin{bmatrix} cos\theta & cos\theta \\ sin\theta & sin\theta \\ -cos\theta & -cos\theta \\ -sin\theta & -sin\theta \end{bmatrix} \tag{28}$$

where θ is the angle between the bond and the x axis at the current configuration. The detailed process for getting these matrices are given in Appendix A.1.

3.3 FEM-PD coupling

To solve the mathematical models described in § 2 using the hybrid FEM-PD approach, we need to effectively deal with two types of coupling: (1) the coupling between PD and FEM and (2) the coupling between the solid deformation and the fluid pressure. The former is reflected by the coupled FEM-PD spatial discretisation of porous media, while the latter is reflected by the coupled fluid and solid equations, see § 2.1 and § 2.2 for details. In this section, we focus on the FEM-PD coupling, while the numerical treatment for fluid-solid coupling will be explained in § 3.4.

Both FEM and PD are used to solve the deformation of porous media. Due to the non-local feature of PD, the application of boundary conditions for peridynamics need to follow specific rules

Table 1: The application of boundary conditions for peridynamics.

Boundary condition	Traction boundary condition	Displacement or velocity boundary condition
Rules	To be applied as body force density in a “real material layer” along the boundary of a nonzero volume.	To be applied by prescribing constraints on displacement and velocity fields in a “fictitious material layer” along the boundary of a nonzero volume.

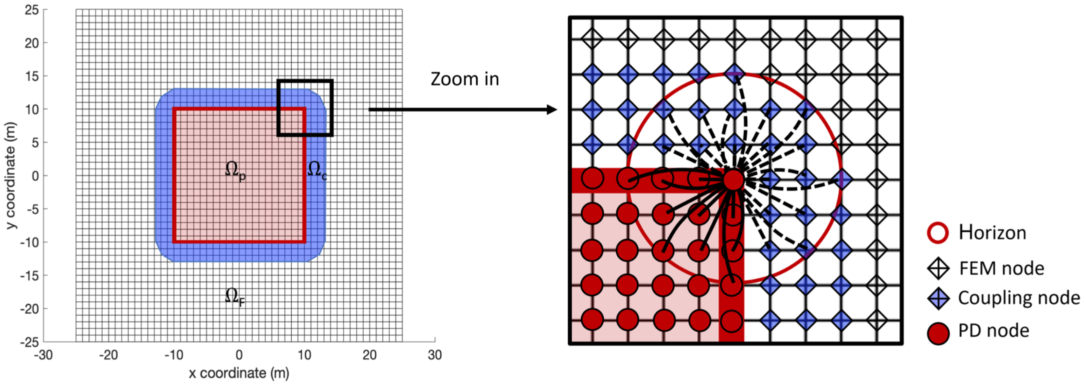

Fig. 3. Illustration of FEM and PD sub-domain.

[39], see Table 1. In this research, FEM is adopted for the outer area, and PD is adopted for the inner area where cracks are likely to occur. The coupling approach described in references [76, 51, 29] is adopted, which is explained as follows. As shown in Fig. 3, the porous media Ω is discretised into FEM sub-domain Ω_F and PD sub-domain Ω_P such that

$$\Omega = \Omega_F + \Omega_P, \quad \Omega_F \cap \Omega_P = \varnothing \tag{29}$$

The nodes in a PD sub-domain are called the PD nodes (red circles), while the nodes in a FEM sub-domain are called the FE nodes (blue and white diamonds). Since the FE nodes shown as blue diamonds (in Fig. 3) are used to define the appropriate internal forces on the real PD nodes (red circles), we call these FE nodes the coupling nodes. The dashed lines represent the bonds coupling PD nodes to the surrounding FE elements. The continuous lines represent standard bonds between PD nodes. The bonds connecting PD nodes to coupling nodes only apply forces to PD nodes while the FE elements having PD nodes only apply forces to FE nodes. The coupling is realised by adopting in the global matrix the terms coming from the FEM, representing forces acting on FE nodes, and the terms coming from the PD discretization, representing forces acting on PD nodes [29]. This coupling ensures the completeness of the integral of the non-local strain energy for all PD nodes and the smooth transition from the local model to the non-local model [51].

3.4 Time discretisation

The coupled fluid-solid equations for crack branching in porous media are dynamic and nonlinear. Here the Newmark method [47] is used for time discretisation taking into account the inertial force and the acceleration terms, and the resulting system is given below:

$$\begin{cases} \ddot{\mathbf{u}}^{n+1} = a_0(\mathbf{u}^{n+1} - \mathbf{u}^n) - a_2\dot{\mathbf{u}}^n - a_3\ddot{\mathbf{u}}^n \\ \dot{\mathbf{u}}^{n+1} = a_1(\mathbf{u}^{n+1} - \mathbf{u}^n) - a_4\dot{\mathbf{u}}^n - a_5\ddot{\mathbf{u}}^n \\ \mathbf{p}^{n+1} = \mathbf{p}^n + \Delta t(1-\theta)\dot{\mathbf{p}}^n + \theta\Delta t\dot{\mathbf{p}}^{n+1} \end{cases} \tag{30}$$

with

$$\begin{aligned} &a_0 = \frac{1}{\beta\Delta t^2}, \quad a_1 = \frac{\gamma_a}{\beta\Delta t}, \quad a_2 = \frac{1}{\beta\Delta t} \\ &a_3 = \frac{1}{2\beta} - 1, \quad a_4 = \frac{\gamma_a}{\beta} - 1, \quad a_5 = \Delta t(\frac{\gamma_a}{2\beta} - 1) \end{aligned} \tag{31}$$

$$\bar{\mathbf{M}}\ddot{\mathbf{u}}^{n+1} + \bar{\mathbf{K}}\mathbf{u}^{n+1} - \bar{\mathbf{Q}}\mathbf{p}^{n+1} = \bar{\mathbf{f}}^{n+1} \tag{32a}$$

$$\mathbf{Q}_F^T\dot{\mathbf{u}}^{n+1} + \mathbf{C}_F\dot{\mathbf{p}}^{n+1} + \mathbf{H}_F\mathbf{p}^{n+1} = \mathbf{q}_F^{n+1} \tag{32b}$$

where $\bar{\mathbf{M}}$ is obtained by assembling $\mathbf{M}_{PD}$ and $\mathbf{M}_F$, $\bar{\mathbf{K}}$ by assembling $\mathbf{K}_F$ and $\mathbf{K}_{PD}$, $\bar{\mathbf{Q}}$ by assembling $\mathbf{Q}_F$ and $\mathbf{Q}_{PD}$, and $\bar{\mathbf{f}}$ by assembling $\mathbf{f}_F$ and $\mathbf{f}_{PD}$.

After substituting Eq. (30) into Eq. (32), we obtain the following equation system:

$$\begin{Bmatrix} \mathbf{u} \\ \mathbf{p} \end{Bmatrix}^{(n+1)} = \begin{Bmatrix} \mathbf{u} \\ \mathbf{p} \end{Bmatrix}^{(n)} - \frac{\mathbf{R}}{\mathbf{J}} \tag{33}$$

$$\mathbf{J} = \begin{bmatrix} a_0\bar{\mathbf{M}} + \bar{\mathbf{K}} & -\bar{\mathbf{Q}} \\ a_1\mathbf{Q}_F^T & \dfrac{\mathbf{C}_F}{\theta\Delta t} + \mathbf{H}_F \end{bmatrix} \tag{34}$$

$$\mathbf{R} = \begin{bmatrix} \bar{\mathbf{M}}(a_0(\mathbf{u}^{n+1} - \mathbf{u}^n) - a_2\dot{\mathbf{u}}^n - a_3\ddot{\mathbf{u}}^n) + \bar{\mathbf{K}}\mathbf{u}^{n+1} - \bar{\mathbf{Q}}\mathbf{p}^{n+1} - \bar{\mathbf{f}}^{n+1} \\ \mathbf{Q}_F^T(a_1(\mathbf{u}^{n+1} - \mathbf{u}^n) - a_4\dot{\mathbf{u}}^n - a_5\ddot{\mathbf{u}}^n) + \mathbf{C}_F \cdot \dfrac{\mathbf{p}^{n+1} - \mathbf{p}_w^n - \Delta t(1-\theta)\dot{\mathbf{p}}_w^n}{\theta\Delta t} + \cdots \\ \mathbf{H}_F\mathbf{p}^{n+1} - \mathbf{q}^{n+1} \end{bmatrix} \tag{35}$$

When $\gamma_a \geq 1/2$, $\beta \geq 1/4$, and $\theta \geq 1/2$, the above equation system is unconditionally stable. The coupled nonlinear equation system is solved via a monolithic scheme with the Newton-Raphson method.

3.5 Simulation flowchart

The simulation flow chart for solving the dynamic failure problem with the FEM-PD method is illustrated in Fig. 4. After the initial and boundary conditions are given, the domain is divided into the FEM sub-domain and PD sub-domain following the rule that the crack is assumed to develop in the PD sub-domain. Then, the coupled matrix is assembled using the PD matrix and FEM matrix coupling strategy. The Newmark method is used for time discretisation, further details can be found in § 3.4. For each time step if local failure is detected ($s \geq s_c$ in Eq. (18)), dynamic crack propagation develops and local bonds break accordingly, forming a nonlinear equation system. The stiffness matrix is updated according to the change in local connectivity whenever broken bonds are detected. Newton iteration is then used to solve the non-linear system. The loop continues until bond breaking has ceased and the result satisfies the convergent condition $error < \epsilon$. Here, $error = \left|\frac{x^{itn+1} - x^{itn}}{x^{itn+1}}\right|$, where x represents the unknowns (pressure or displacements in the 2D hydraulic fracturing problem) and itn represents the iteration step. Once the Newton iteration has converged, go to the next time step.

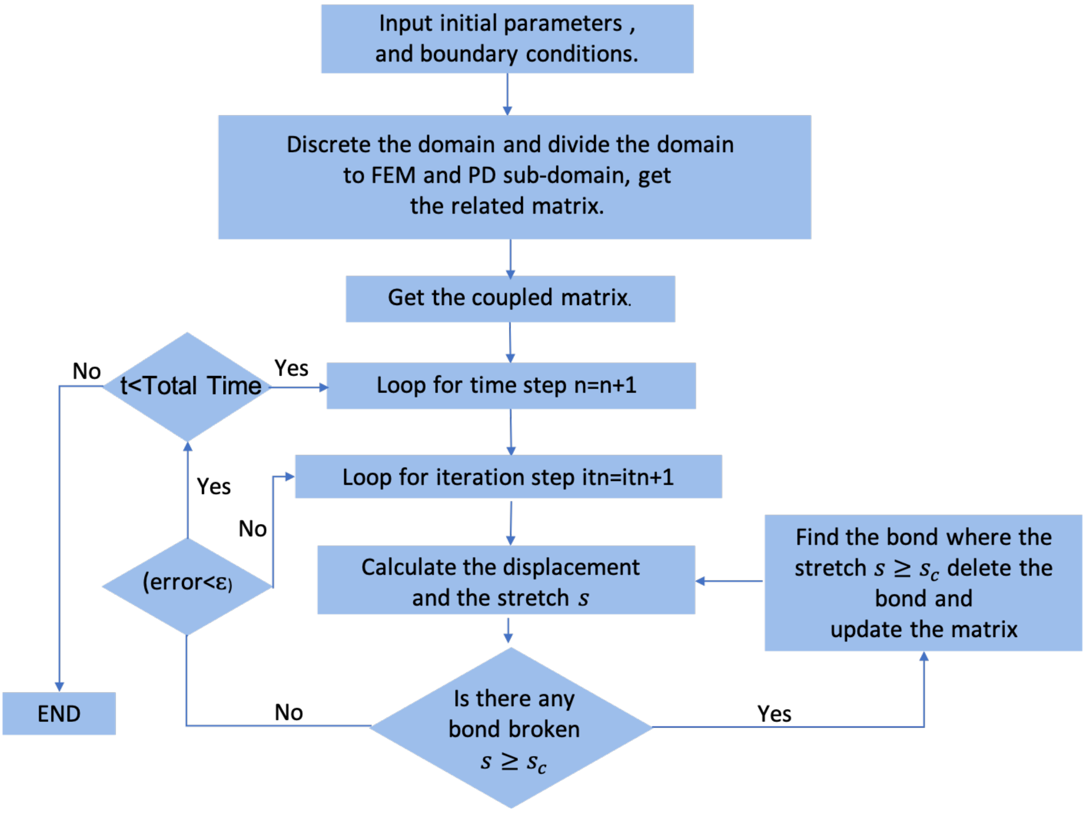

Fig. 4. Flowchart for solving the dynamic failure problem with the FEM-PD method.

4 Model verification

The mathematical models for the deformation, flow and fracture in porous media are all well established individually, so do the FEM and PD formulations. However, due to the FEM-PD coupling and the fluid-solid coupling involved in the numerical solution strategy described in § 3, it is necessary to carefully verify the numerical scheme before applying it to investigate hydraulic fracture branching in porous media. Specifically, three benchmark cases are considered in this section for model verification: a 1D porous media bar, a KGD problem, and a fluid-driven fracture interaction with natural cracks.

4.1 1D porous media bar

The model describes a fully saturated 1D poroelastic column bar with a pressure applied at the top of the bar, see Fig. 5. The height of the column is 15 m. The top surface is subjected to a constant pressure of 10^4 Pa. The top surface is used for fluid drainage and the pore pressure at the top surface remains zero, while the bottom surface acts as a solid wall and the fluid flux is zero. The PD is used to describe the deformation of the porous media and the FEM is used to describe the fluid flow in the porous media. Referring to [52], the material properties are listed in Table 2. To check the convergence, three different grid spacings are considered: (1) $\Delta x = 0.2$ m; (2) $\Delta x = 0.1$ m and (3) $\Delta x = 0.05$ m, where Δx is the grid spacing. The horizon size δ is equal to $3\Delta x$.

The analytical solution to this problem is given in [73]:

$$P(z,t) = \frac{4vP_0}{\pi} \sum_{m=0}^{N} \left\{ \frac{1}{2m+1} \exp(-(\frac{(2m+1)\pi}{2L})^2 ct) \times \sin(\frac{(2m+1)\pi z}{2L}) \right\} \tag{36}$$

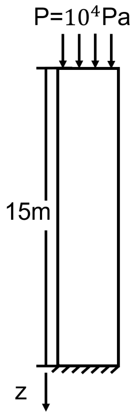

Fig. 5. The geometry of 1D porous media bar model.

Table 2: Material properties for the poroelastic column.

Properties	Symbols	Values
Elasticity modulus	E	1.0×10^8 Pa
Biot coefficient	α	0.5
Biot modulus	Q	6.06×10^9 N/m^2
Viscosity	μ	1.0×10^{-3} Pa $\cdot$ s
Permeability	k	1.0×10^{-12} m^2
Material density	ρ	1.9×10^3 kg/m^3

$$\begin{aligned} u(z,t) =& c_m v P_0 \left\{ (L-z) - \frac{8L}{\pi^2} \sum_{m=0}^{N} \left\{ \frac{1}{(2m+1)^2} \right\} \right\} \times \exp(-(\frac{(2m+1)\pi}{2L})^2 ct) \\ & \times \cos(\frac{(2m+1)\pi z}{2L}) + a_i P_0 (h-z) \end{aligned} \tag{37}$$

where

$$v = \frac{a-a_i}{\alpha a}, \quad a_i = \frac{a}{1+\alpha^2 a Q}, \quad c = \frac{kQ}{(\alpha^2 a + Q)\mu}, \quad c_m = (a-a_i)/v \tag{38}$$

with $a = 1.0 \times 10^{-8}$ N/m^2.

Fig. 6 shows the distributions of pore pressure and displacement along the central axis at different times with different grid sizes. The numerical solutions show good agreement with the analytical solutions and with smaller grid size, the numerical results indicate convergence towards the analytical results. As time increases, the pore pressure decreases and the displacement increases in z direction, indicating water out flow from the top surface together with soil consolidation.

4.2 KGD problem

As shown in Fig. 7, a plane strain KGD problem [15] is employed to examine the hybrid numerical scheme in two-dimensions. The borehole is treated as a point source in the plane because the radius is very small compared to the fracture length. Due to symmetry, Fig. 7 only shows half of the model, which is 16 m in height and 8 m in width. The domain is divided into a FEM-subdomain and a PD-subdomain, where the PD-subdomain is the area where the crack can potentially occur. The PD sub-domain is 8 m $\times$ 8 m, as indicated by the red rectangle in Fig. 7.

For boundary conditions, the top and bottom sides are fixed in the vertical direction, the right edge is fixed in the horizontal direction, and the pressure on the boundaries is set as zero. The initial crack

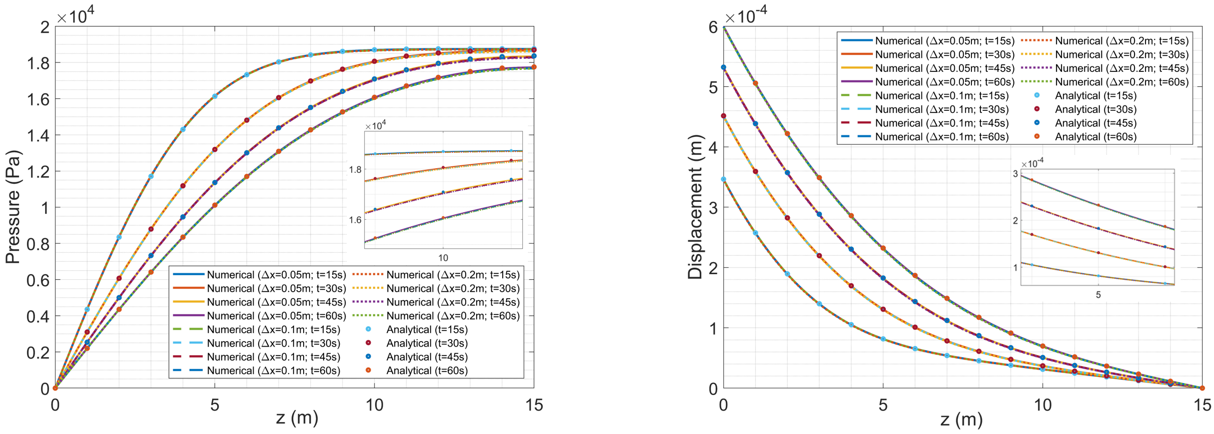

(a) Pressure distribution.

(b) Displacement distribution.

Fig. 6. Comparison of analytical and numerical solutions along the bar.

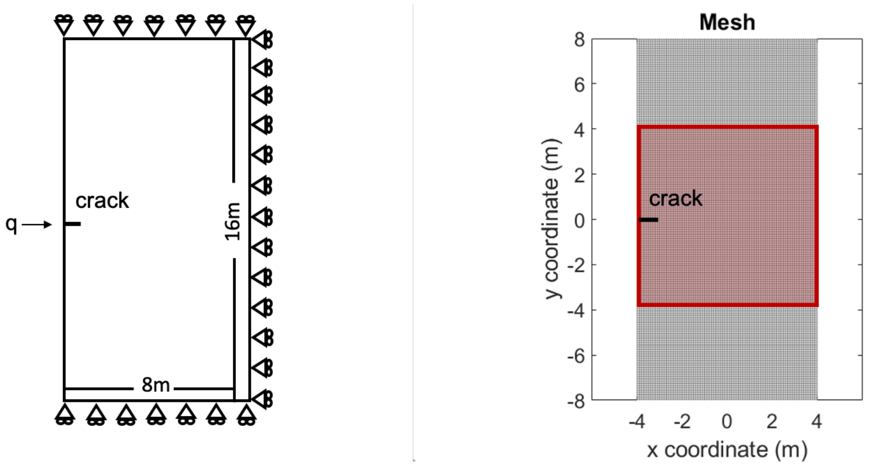

Fig. 7. Geometry and discretisation of the KGD model

length is 0.1 m and a flux $q = 0.0001$ m^3/s is injected in the left borehole. The rock media is assumed homogeneous and fully saturated, and it undergoes small deformation. All parameters including the rock properties, fluid properties and other conditions used in the numerical simulation are listed in Table 3. Note that for the element inside the fracture domain, the porosity is 1 and the permeability is calculated using Eq. (16) and Eq. (17).

In order to check for convergence of the results, three different grid spacings and time steps are used: (1) $\Delta x = 0.2$ m, $\Delta t = 0.2$ s; (2) $\Delta x = 0.1$ m, $\Delta t = 0.1$ s and (3) $\Delta x = 0.05$ m, $\Delta t = 0.05$ s. The horizon size δ is equal to $3\Delta x$. The comparison between the analytical solutions [31, 69] and numerical results in terms of evolution of the fracture length, pressure and width are shown in Fig. 8. Using $\Delta x = 0.05$ m and $\Delta t = 0.05$ s, the growth of crack and the distribution of pressure in porous media and in the fracture are shown in Fig. 9.

All three parameters show convergence with accuracy increasing with the decrease of time step and mesh size, which demonstrates the reliability of the numerical method for hydraulic fracturing problems. However, we note that while errors are decreasing the largest errors are in the evolution of the fluid pressure and fracture width at the borehole. There are two potential causes for this difference. First, the analytical solution is based on the local theory while the numerical solution is established on non-local theory (peridynamics). Secondly, the medium in the analytical solution is linearly elastic and there is no leak-off at the fracture surface, while in our model, the medium is poroelastic and the fracture surface is permeable since the leak-off is automatically captured by the model.

Table 3: Rock properties, fluid properties and loading conditions used in KGD simulation.

Properties	Symbols	Values
Elasticity modulus	E	15.96×10^9 Pa
Poisson's ratio	v	0.25
Biot coefficient	α	1
Bulk modulus(Solid)	K_s	36×10^9 Pa
Bulk modulus(Fluid)	K_f	3×10^9 Pa
Viscosity	μ	1.0×10^{-3} Pa $\cdot$ s
Material density	ρ	1.81×10^3 kg/m^3
Porosity	n	0.19
Permeability	k	1.0×10^{-14} m^2
Critical energy release rate	G_c	100 N/m

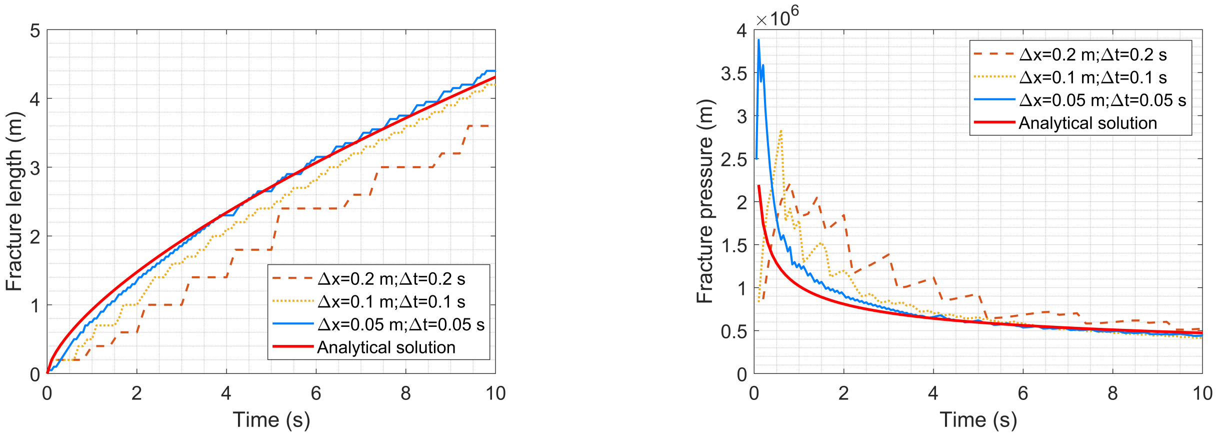

(a) Fracture length evolution.

(b) Fracture pressure evolution.

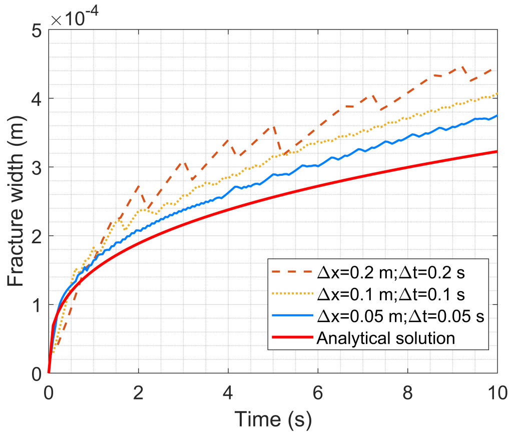

(c) Fracture width evolution.

Fig. 8. Verification of the KGD model.

4.3 Fluid-driven fracture interaction with natural cracks

To test the method capability of describing multiple cracks and evaluating fluid pressure in and out of the fracture area, a problem involving a fluid-driven fracture interacting with natural cracks [80] is considered. With the exception of an additional natural crack, the geometry of the model is similar to that of the KGD model. The natural crack is 4 m long and 3.8 m away from the original crack that is 0.2 m in length. The domain is divided into an FEM-subdomain and a PD-subdomain, where the

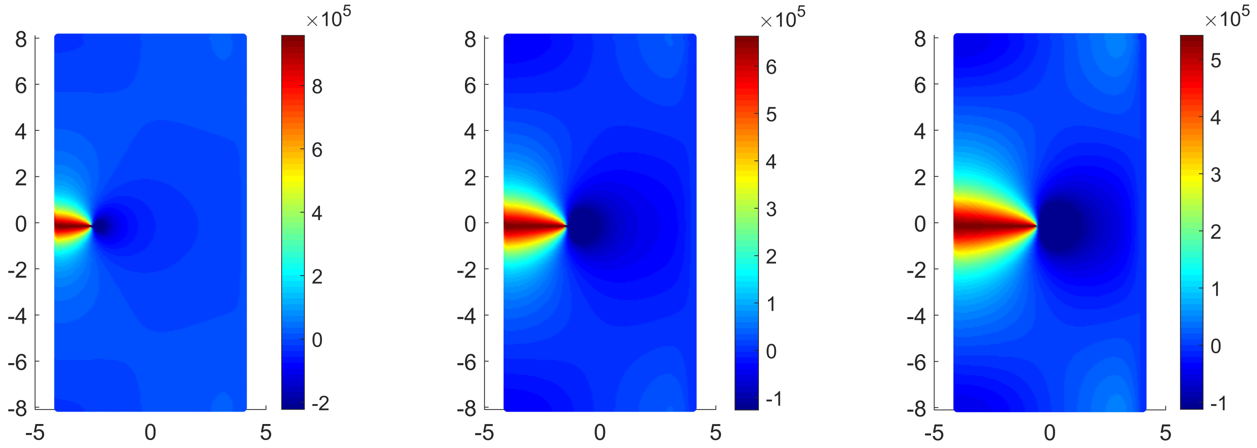

(a) t=2.5 s. **(b)** t=5 s. **(c)** t=7.5 s.

Fig. 9. Pore pressure and fracture pressure distribution with time varying (unit: Pa).

PD-subdomain is 8 m $\times$ 12 m, as indicated by the red rectangle in Fig. 10.

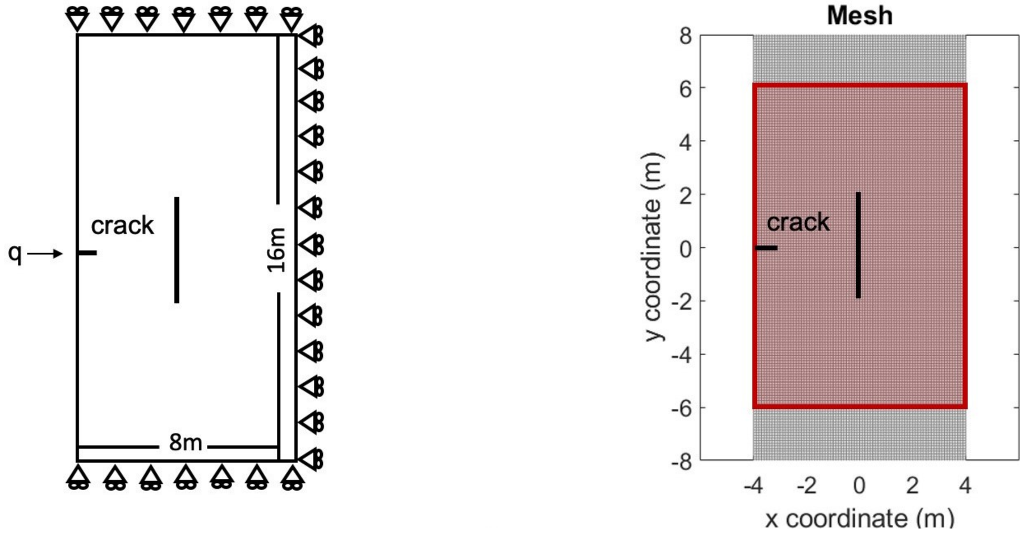

Fig. 10. Geometry and discretisation of fracture interaction model.

The boundary conditions and material properties are listed in Table 3, together with a flux of $q = 0.0001$ m^3/s applied. The time step Δt is set to 0.1 s. The fracture path evolution with time t is shown in Fig. 11. The time varying pressure distribution in and out of the fracture is shown in Fig. 12.

Both the fracture path and the pressure results are in good agreement with the literature [52, 80]. Initially, the fracture propagates in the horizontal direction. Fluid is injected in the borehole as time evolves and the fracture starts to interact with the natural crack (the vertical crack in Fig. 10), and the fluid starts to flow along the vertical direction. Due to the interaction between the cracks, the crack propagation direction changes. Model verification demonstrates that the proposed method can describe hydraulic fracturing propagation in porous media in a relatively straight forward way.

5 Dynamic branching study

The simulation results of hydraulic fracture branching are influenced by many factors, which can essentially be divided into two types: physical and non-physical factors. Physical factors refer to properties of porous media and operational conditions, and non-physical factors refer to assumptions

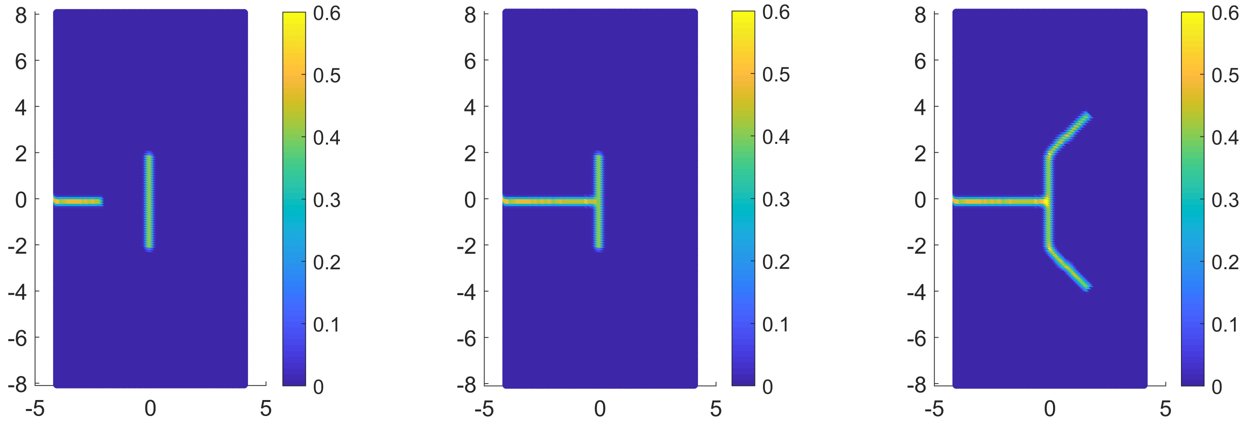

(a) $t = 3.5$ s. **(b)** $t = 13.5$ s. **(c)** $t = 62.5$ s.

Fig. 11. Fracture path evolution with time varying.

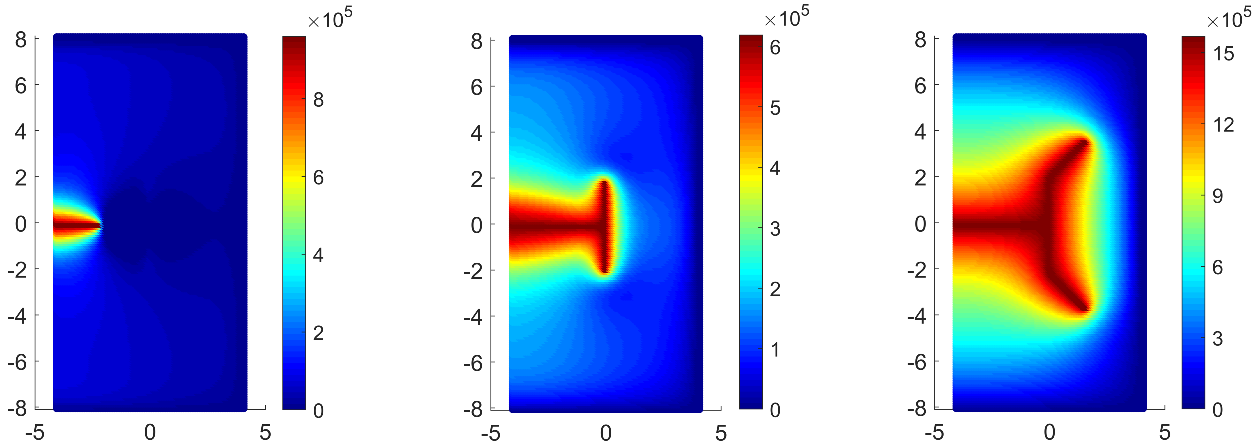

(a) $t = 3.5$ s. **(b)** $t = 13.5$ s. **(c)** $t = 62.5$ s.

Fig. 12. Pore pressure and fracture pressure distribution with time varying (unit: Pa).

made in the mathematical model or method itself. As discussed in § 1, the physical factors mainly include Young's modulus, in-situ stress condition, injection rate, viscosity, porosity and permeability, energy release rate and heterogeneity. Until now, how they affect hydraulic fracture branching has not been systematically investigated, while the conclusions from related studies by different authors are not always consistent, see Table 4. In the effort to bridge this gap, we use the proposed hybrid FEM-PD model to study the sensitivity of different physical parameters to the branching phenomenon.

Specifically, six parameters are selected in this study: the flux rate, Young's modulus, porosity, permeability, viscosity, and energy release rate. The influence of in-situ stress and heterogeneity is not included here because all models and field and experimental results reach a consensus on this point, namely, low in-situ stress difference and heterogeneity is beneficial for crack branching. In addition, to reduce the complexity and ensure the uniqueness of variables, the influence of non-physical factors is eliminated in this study. In peridynamics, the grid size, the horizon size and micro-modulus function model all have an influence on the crack geometry and crack branch [8, 18]. In order to reduce the dependence of crack paths on grid and capture the crack branching behavior accurately [25], an m ratio of $m = 4$, namely the ratio between the horizon and the grid spacing, is

Table 4: Comparison between the previous conclusions and our conclusions.

Physical Factors	Existing conclusions	Our conclusions
Flux rate	Faster flux rate leads to branching phenomenon. (1) Secondary branching is observed with increasing flux (hybrid FEM-PD model) [52] (2) No secondary branching is observed with increasing flux and flux rate has little effect on final crack patterns (PFM) [80]	Faster flux rate leads to branching phenomenon, no secondary branching is observed and branching angles increases with increasing flux rate
Young's modulus	Branching occurs when the crack propagates into rock with high Young's modulus (PFM) [32]	Multiple branches are observed with higher Young's modulus
Porosity	No porosity, no branching phenomenon (finite element crack band model) [56]	Porosity has a limited effect on branching phenomenon, with higher porosity, the branching angles slightly decrease
Permeability	(1) No permeability, no branching phenomenon (finite element crack band model) [56] (2) The permeability has limited effect on crack propagation direction (PFM) [49]	Lower permeability is beneficial to crack branching
Viscosity	(1) Lower viscosity is beneficial to crack branching [52] (2) In homogeneous rock, the fluid with lower viscosity exerts little influence on fracture complexity (lattice Boltzmann method (LBM) - discrete element method (DEM) coupled model) [19]	Effects of viscosity to branching phenomenon is multifacet.
Energy release rate	Lower energy release rate leads to branching phenomenon (PFM) [80]	Lower energy release rate leads to branching phenomenon, secondary branching is observed with decreasing energy release rate

adopted. The grid size and micro modulus function keeps constant and the horizon size is set to be $\delta = 4\Delta x (\Delta x = 0.075m)$. The results from this work and various literatures are compared in Table 4, which shows both agreement and differences and are discussed in the following subsections.

5.1 Effect of flux rate

The effect of flux rate on crack branching is investigated and discussed in this subsection. The geometry and the boundary conditions are the same as that used in the KGD model. Three different cases are studied with three different flux rates, namely, case 1-1 ($q = 0.001$ m^3/s), case 1-2 ($q = 0.005$ m^3/s), case 1-3 ($q = 0.01$ m^3/s). The other parameters are unchanged, see Table 3. The crack patterns under different flux rate are shown in Fig. 13. As expected, as the flux rate increases, the crack starts to branch. With the flux rate increasing, the fluid velocity increases together with the energy that drives the fracture. When the energy is much higher than what the porous media can dissipate, the crack starts to branch. A secondary crack branching phenomenon with increase in flux rate is not observed in our model. However, with increasing flux rate, the crack angle increases, which is also observed in [80]. Fig. 14 shows the fluid pressure under different flux rate at the injection point. As observed, a higher flux rate will cause a larger fluid pressure. The pressure oscillation occurs because it is influenced by the mesh size (see Fig. 8b) and the interacting velocities: the velocity of the crack advancement, the velocity of the fluid in the fracture and the seepage velocity of the fluid in the domain and from the crack [13].

5.2 Effect of Young's modulus

With a fixed high flux rate $q = 0.01$ m^3/s, the influence of Young's modulus on crack branching is investigated. Typical values of Young's modulus for rock formations range from 20 GPa to about 40 GPa [74]. Thus, three different cases are investigated here, which are marked as: case 2-1 ($E = 15.96$ GPa), case 2-2 ($E = 23.94$ GPa), case 2-3 ($E = 31.92$ GPa). The other parameters are unchanged. Fig. 15 shows the crack patterns resulting from different Young's modulus. With the increase in Young's modulus, the crack angle becomes smaller and the crack patterns become complex, even secondary crack branching can be observed. There are two possible reasons behind this phe-

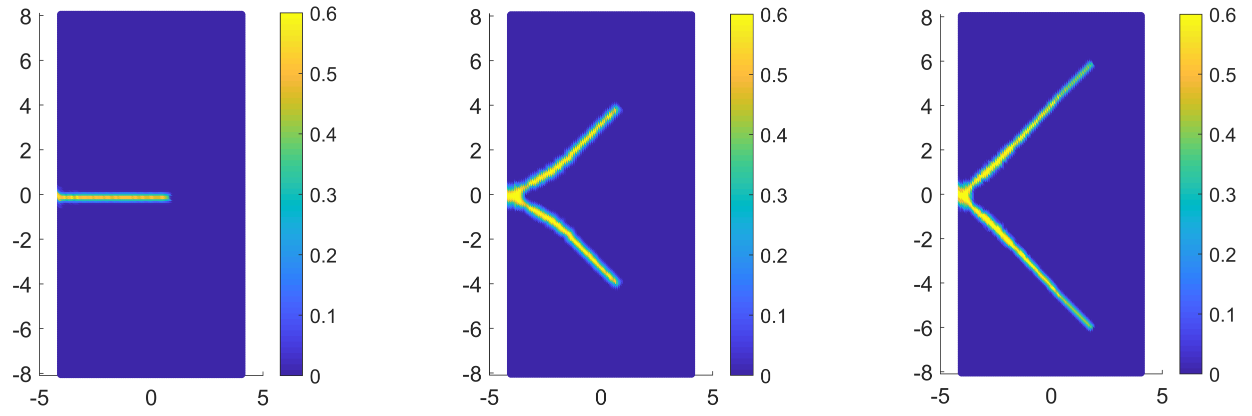

(a) Case 1-1 ($q = 0.001$ m^3/s). **(b)** Case 1-2 ($q = 0.005$ m^3/s). **(c)** Case 1-3 ($q = 0.01$ m^3/s).

Fig. 13. Crack patterns under different flux rate.

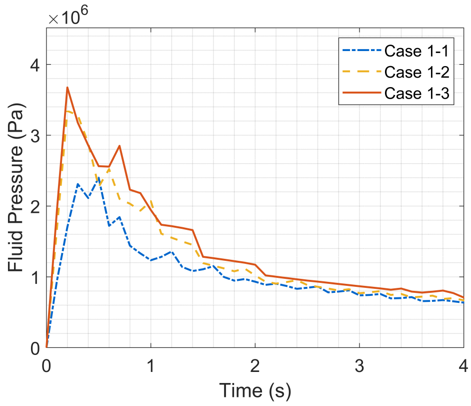

Fig. 14. The variation of pressure under different flux rate.

nomenon. First, since the Young's modulus describes the ability of the material to resist deformation, rocks with low Young's modulus tend to be ductile and rocks with high Young's modulus tend to be brittle [38]. Cracks with sharp tips propagate easier than cracks having blunt tips [12]. Secondly, the value of critical stretch s_c, marked as the crack propagation (bond-break) criterion, is calculated from the value of Young's modulus, see Eq. (19). Therefore, if the Young's modulus is increased, the criterion for crack development decreases, which results in more branches. The variation of pressure value at injection point under different Young's modulus is presented in Fig. 16. For a smaller Young's modulus, the fluid pressure will be smaller.

5.3 Effect of porosity and permeability

In geology, the porosity is the fraction of bulk volume of the reservoir that is not occupied by the solid framework of the reservoir and the permeability describes reservoir rock's ability to allow the fluids to flow through its interconnected pores [71]. They are closely related to each other [20]. So we study these two factors in the same section.

The porosity values for sedimentary rocks reservoirs range from 0.1 to 0.4 in sandstones and from 0.05 to 0.5 in carbonates [21]. Thus, with a flux rate $q = 0.01$ m^3/s, three cases are selected: case 3-1 ($n = 0.2$), case 3-2 ($n = 0.3$), case 3-3 ($n = 0.4$). For permeability, since ($k = 1.0 \times 10^{-14}$ m^2) is already very small, an increasing permeability scheme is selected. Three cases including case 4-1 ($k = 1.0 \times 10^{-14}$ m^2), case 4-2 ($k = 1.0 \times 10^{-13}$ m^2), case 4-3 ($k = 1.0 \times 10^{-12}$ m^2) are tested with the porosity $n = 0.2$ and the flux rate $q = 0.01$ m^3/s. The effect of different porosity and permeability

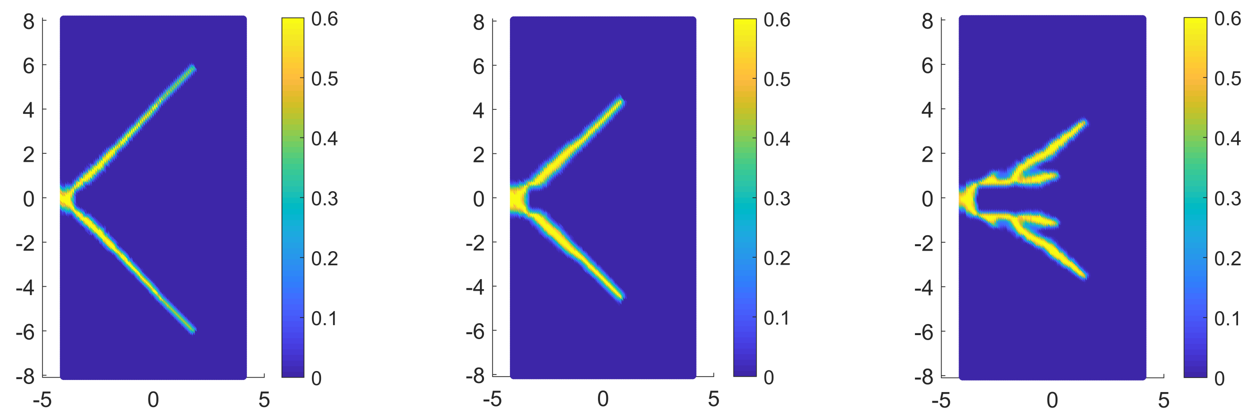

(a) Case 2-1 ($E = 15.96$ GPa). **(b)** Case 2-2 ($E = 23.94$ GPa). **(c)** Case 2-3 ($E = 31.92$ GPa).

Fig. 15. Crack patterns under different Young's modulus.

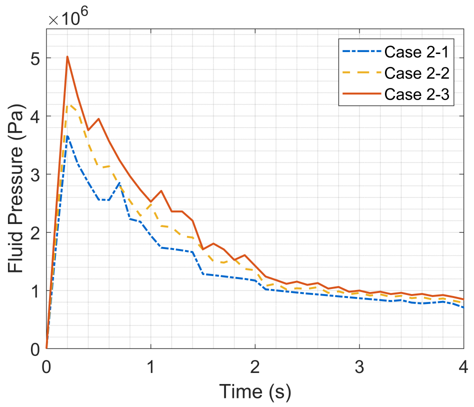

Fig. 16. The variation of pressure under different Young's modulus.

on crack branching is studied. Fig. 17 and Fig. 18 show the crack patterns under different porosity and permeability, separately.

From Fig. 17 and Fig. 18, it can be observed that compared with porosity, the branching phenomenon is much more sensitive to permeability. With higher porosity, the crack branching angle slightly decreases. However, with higher permeability, the crack patterns change significantly, the crack develops a much smaller branching angle, and propagates along a straight line instead of branching. The reason is most likely due to the permeability increase, which results in more fluid flow into the porous media, and consequently in less fluid flowing into the fracture, so that the energy driven by the fluid in the fracture becomes smaller and the crack propagation velocity decreases. Fig. 19 and Fig. 20 show fluid pressure at the injection point for different porosity and permeability. It can be observed that the porosity has little effect on fluid pressure at the injection point while the fluid pressure decreases with the increase of permeability.

5.4 Effect of viscosity

To study the effect of different viscosity on hydraulic crack branching, parameters in Table 3 are modified here to make the propagation scheme belong to viscosity dominated regime [63]. The energy release rate is modified to $G = 1$ N/m and the flux rate is set as $q = 0.001$ m^3/s. The other parameters remain unchanged. Three different viscosity, namely, case 5-1 ($\mu = 0.1$ Pa·s), case 5-2 ($\mu = 0.01$ Pa·s), case 5-3 ($\mu = 0.001$ Pa·s) are examined. The crack patterns under different viscosity are shown in Fig. 21. By decreasing the fluid viscosity from $\mu = 0.1$ Pa·s to $\mu = 0.01$ Pa·s, the branching

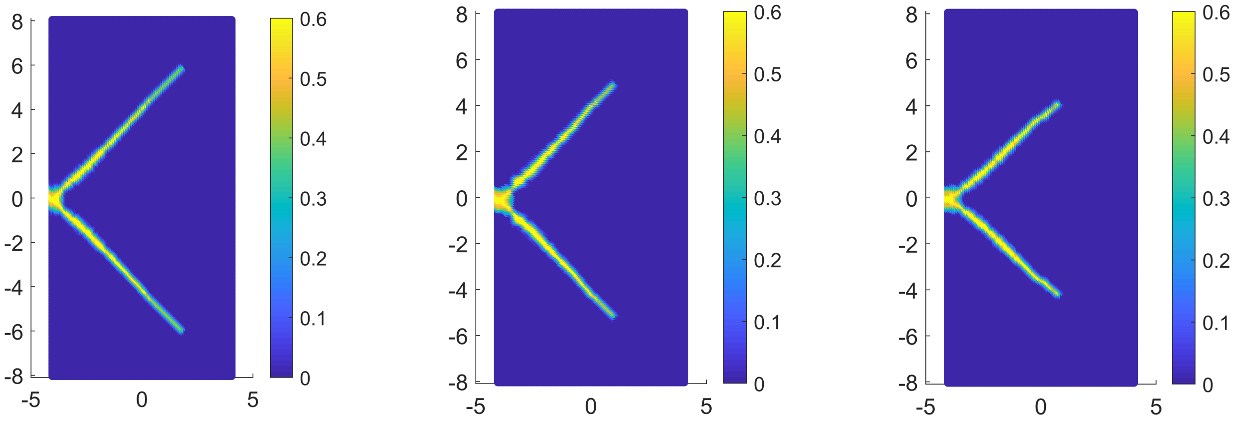

(a) Case 3-1 ($n = 0.2$).

(b) Case 3-2 ($n = 0.3$).

(c) Case 3-3 ($n = 0.4$).

Fig. 17. Crack patterns under different porosity.

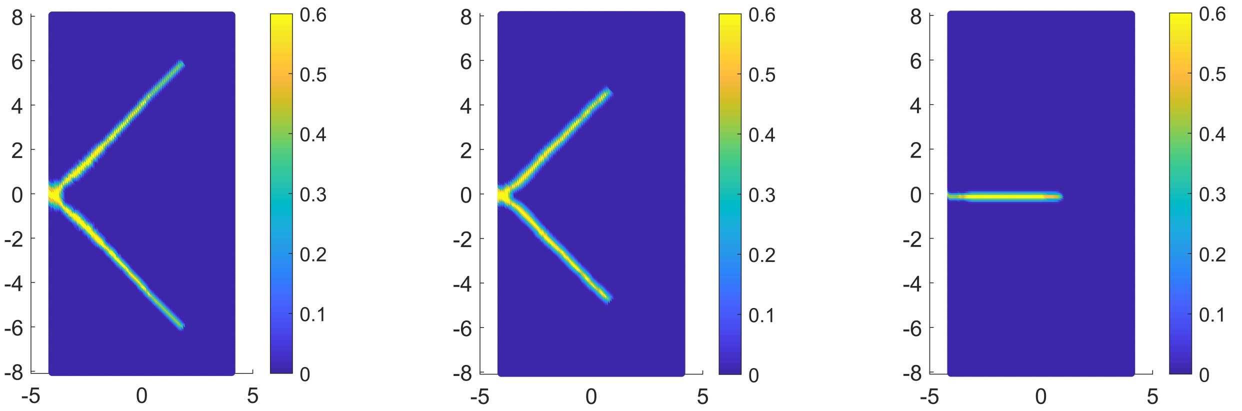

(a) Case 4-1 ($k = 1.0 \times 10^{-14}$ m^2).

(b) Case 4-2 ($k = 1.0 \times 10^{-13}$ m^2).

(c) Case 4-3 ($k = 1.0 \times 10^{-12}$ m^2).

Fig. 18. Crack patterns under different permeability.

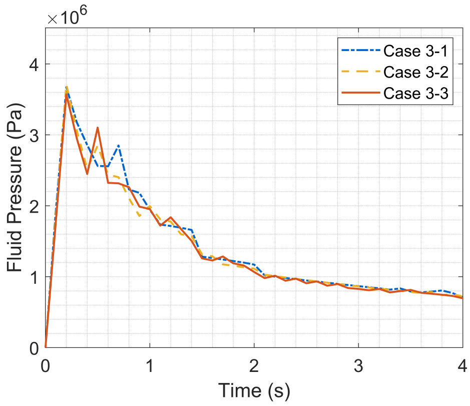

Fig. 19. The variation of pressure under different porosity.

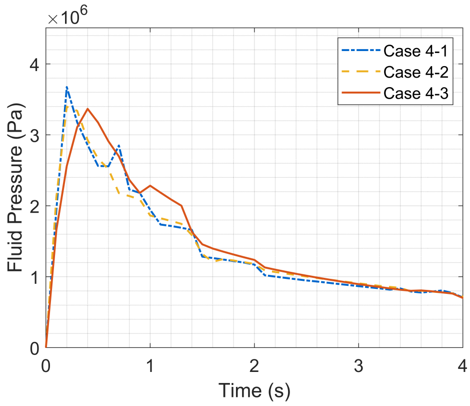

Fig. 20. The variation of pressure under different permeability.

angle grows. This phenomenon is also observed by increasing the flux rate, which indicates that increasing the flux rate or decreasing the viscosity may cause a similar effect. This is consistent with what has been observed in numerical and experimental results: complex fracture patterns are prone to form with lower viscosity and high flux rate [52, 65, 77]. However, when the viscosity varies from $\mu = 0.01$ Pa·s to $\mu = 0.001$ Pa·s, the increasing angles phenomenon becomes less obvious. A likely reason is that: due to the propagation of the fracture is a complex interaction process between the solid formation and the fluid, the effect of viscosity on hydraulic fracturing is multifaceted. Reducing viscosity will increase the velocity of the fluid, thereby enhancing the hydraulic driving force. Increasing the intrinsic permeability of the porous media causes more fluid to flow into the porous media, so the hydraulic driving force is reduced. The variation of pressure value at injection point under different viscosity is plotted in Fig. 22, from which it can be observed that higher viscosity will cause higher fluid pressure at the injection point.

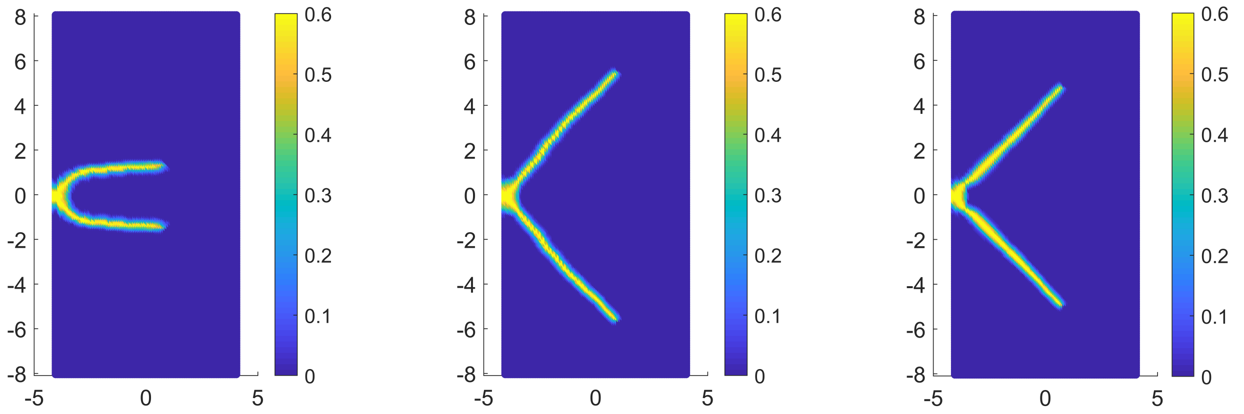

(a) Case 5-1 ($\mu = 0.1$ Pa·s). **(b)** Case 5-2 ($\mu = 0.01$ Pa·s). **(c)** Case 5-3 ($\mu = 0.001$ Pa·s).

Fig. 21. Crack patterns under different viscosity.

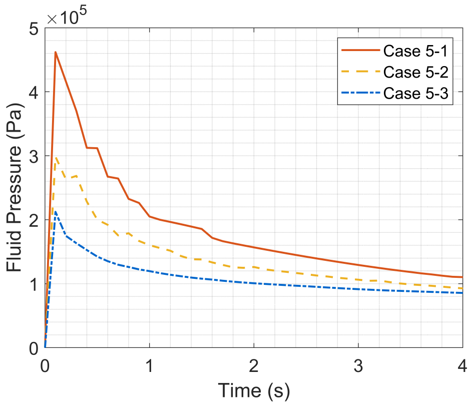

Fig. 22. The variation of pressure under different viscosity.

5.5 Effect of energy release rate

With the viscosity $\mu = 0.001$ Pa·s, the flux rate $q = 0.0001$ m^3/s and the other parameters fixed, the effect of energy release rate is investigated with three different cases: case 6-1 ($G = 1$ N/m), case 6-2 ($G = 0.01$ N/m), case 6-3 ($G = 0.001$ N/m). The crack patterns under different energy release rates are shown in Fig. 23. As expected, by decreasing the energy release rate, the crack branching phenomenon can be observed. When the energy release rate is sufficiently low, the complex crack patterns, e.g. secondary crack branching, are prone to form. We note that the thicknesses of some parts of the crack patterns are abnormally large, which may be caused by the widening damage process-zone before crack branching due to the increasing fracture roughness [57, 58] and the simultaneous breaking of a series of bonds due to the change of the physical parameters (e.g. energy release rate) during dynamic simulation. The fluid pressure from the injection point under different energy release rate is compared in Fig. 24, from which it can be concluded that a larger energy release rate causes larger fluid pressure, which is also observed in [80].

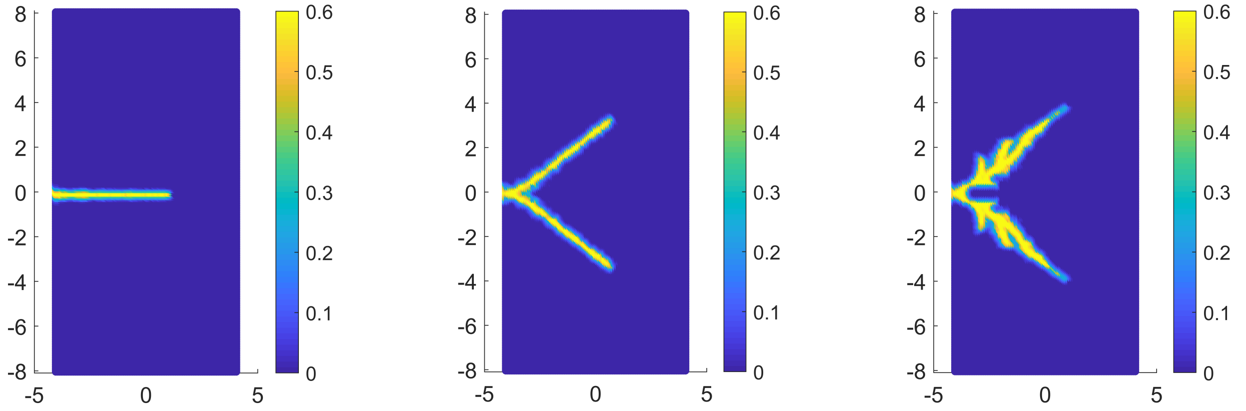

(a) Case 6-1 ($G = 1$ N/m). **(b)** Case 6-2 ($G = 0.01$ N/m). **(c)** Case 6-3 ($G = 0.001$ N/m).

Fig. 23. Crack patterns under different energy release rate.

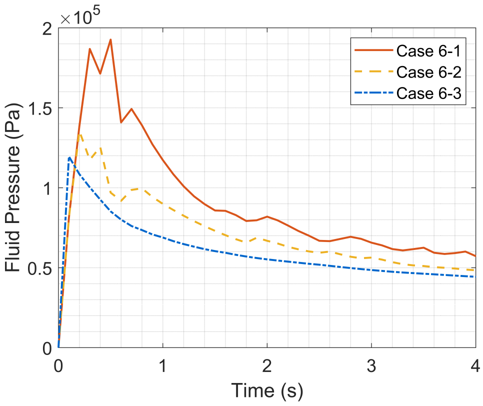

Fig. 24. The variation of pressure under different energy release rate.

6 Conclusions

In this paper, a fully coupled hydraulic fracture propagation simulation method with a hybrid finite element method (FEM) - peridynamics (PD) scheme is presented. The method has been verified with three benchmark examples and proved to be effective for simulating complex dynamic crack propagation. The effects of different factors on branching phenomenon are investigated using the method presented. From the conducted analysis, we find that complex crack patterns are prone to form with faster loading rate, lower energy release rate, and more brittle and impermeable media.

Compared with a staggered solver, the monolithic solver presented here solves for the displacements and pressure simultaneously. The strong coupling between the porous media and growing fractures is captured accurately, and the time step limitation is removed, making this method very competitive for solving hydraulic fracture problems on the geological scale. The bond-based peridynamics adopted here can be extended to an advanced version "state-based peridynamics" to remove the limitations of constraints on fixed Poisson's ratios. The bond-based peridynamics are intentionally chosen here for efficiency and simplicity. Work is in progress to tackle problems with hydraulic fracturing in heterogeneous media.

Acknowledgements

The authors would like to thank the supports from China Scholarship Council (CSC No.: 201709370055), Swansea University (Zienkiewicz Scholarship), and the Royal Society (Ref.: IEC\NSFC\191628).

A Appendices

A.1 Appendix

Take the first term of Eq. (24) as an example, if the assumption "small displacement" is made ($|\boldsymbol{\eta}| \ll |\boldsymbol{\xi}|$), it can be simplified as:

$$\mathbf{f}_{ij} = cs\lambda \frac{\boldsymbol{\eta} + \boldsymbol{\xi}}{|\boldsymbol{\eta} - \boldsymbol{\xi}|} \cong cs\lambda \frac{\boldsymbol{\xi}}{|\boldsymbol{\xi}|} \tag{A.1}$$

According to Eq. (A.1), the derivative of the pairwise force $\mathbf{f}_{ij}$ with respect to $\boldsymbol{\eta}$ is:

$$\frac{\partial f}{\partial \eta_1} = c\lambda \frac{\partial s}{\partial \eta_1} = c\lambda \frac{\partial \left(\frac{\sqrt{(\xi_1+\eta_1)^2 + (\xi_2+\eta_2)^2} - |\boldsymbol{\xi}|}{|\boldsymbol{\xi}|} \right)}{\partial \eta_1} = \frac{c\lambda}{|\boldsymbol{\xi}|} \frac{\frac{1}{2} \cdot 2 \cdot (\xi_1 + \eta_1)}{\sqrt{(\xi_1 + \eta_1)^2 + (\xi_2 + \eta_2)^2}} \tag{A.2}$$

where f is he norm of the vector of $\mathbf{f}_{ij}$, $\boldsymbol{\xi} = (\xi_1, \xi_2)$ and $\boldsymbol{\eta} = (\eta_1, \eta_2)$. Due to the assumption "small displacement", the following relation holds

$$\sqrt{(\xi_1 + \eta_1)^2 + (\xi_2 + \eta_2)^2} \cong |\boldsymbol{\xi}| \tag{A.3}$$

Substituting Eq. (A.3) into Eq. (A.2) yields:

$$\frac{\partial f}{\partial \eta_1} = \lambda \frac{c\xi_1}{|\boldsymbol{\xi}|^2} \tag{A.4}$$

Similarly,

$$\frac{\partial f}{\partial \eta_2} = \lambda \frac{c\xi_2}{|\boldsymbol{\xi}|^2} \tag{A.5}$$

Thus,

$$\mathbf{f}_{ij} = \begin{bmatrix} \frac{\partial f_1}{\partial \eta_1} & \frac{\partial f_1}{\partial \eta_2} \\ \\ \frac{\partial f_2}{\partial \eta_1} & \frac{\partial f_2}{\partial \eta_2} \end{bmatrix} \begin{bmatrix} \eta_1 \\ \eta_2 \end{bmatrix} = \lambda \begin{bmatrix} \frac{c\xi_1}{|\boldsymbol{\xi}|^2} \cdot \frac{\xi_1}{|\boldsymbol{\xi}|} & \frac{c\xi_2}{|\boldsymbol{\xi}|^2} \cdot \frac{\xi_1}{|\boldsymbol{\xi}|} \\ \\ \frac{c\xi_1}{|\boldsymbol{\xi}|^2} \cdot \frac{\xi_2}{|\boldsymbol{\xi}|} & \frac{c\xi_2}{|\boldsymbol{\xi}|^2} \cdot \frac{\xi_2}{|\boldsymbol{\xi}|} \end{bmatrix} \begin{bmatrix} -1 & 0 & 1 & 0 \\ 0 & -1 & 0 & 1 \end{bmatrix} \begin{bmatrix} u_{i1} \\ u_{i2} \\ u_{j1} \\ u_{j2} \end{bmatrix} \tag{A.6}$$

A.2 Appendix

$$\begin{aligned} \mathbf{N}_u &= \begin{bmatrix} \mathbf{N}_1 & 0 & \mathbf{N}_2 & 0 & \cdots & \mathbf{N}_n & 0 \\ 0 & \mathbf{N}_1 & 0 & \mathbf{N}_2 & \cdots & 0 & \mathbf{N}_n \end{bmatrix} \\ \mathbf{N}_p &= \begin{bmatrix} \mathbf{N}_1 & \mathbf{N}_2 & \cdots & \mathbf{N}_n \end{bmatrix} \\ \mathbf{B}_u &= \begin{bmatrix} \mathbf{N}_{1,x} & 0 & \mathbf{N}_{2,x} & 0 & \cdots & \mathbf{N}_{n,x} & 0 \\ 0 & \mathbf{N}_{1,y} & 0 & \mathbf{N}_{2,y} & \cdots & 0 & \mathbf{N}_{n,y} \\ \mathbf{N}_{1,y} & \mathbf{N}_{1,x} & \mathbf{N}_{2,y} & \mathbf{N}_{2,x} & \cdots & \mathbf{N}_{n,y} & \mathbf{N}_{n,x} \end{bmatrix} \\ \mathbf{B}_p &= \begin{bmatrix} \mathbf{N}_{1,x} & \mathbf{N}_{2,x} & \cdots & \mathbf{N}_{n,x} \\ \mathbf{N}_{1,y} & \mathbf{N}_{2,y} & \cdots & \mathbf{N}_{n,y} \end{bmatrix} \end{aligned} \tag{A.7}$$

References

[1] J. Adachi, E. Siebrits, A. Peirce, and J. Desroches. Computer simulation of hydraulic fractures. *International Journal of Rock Mechanics and Mining Sciences*, 44(5):739–757, 2007.

[2] A. Agwai, I. Guven, and E. Madenci. Predicting crack propagation with peridynamics: a comparative study. *International journal of fracture*, 171(1):65, 2011.

[3] G. M. Atkinson, D. W. Eaton, H. Ghofrani, D. Walker, B. Cheadle, R. Schultz, R. Shcherbakov, K. Tiampo, J. Gu, R. M. Harrington, et al. Hydraulic fracturing and seismicity in the western canada sedimentary basin. *Seismological research letters*, 87(3):631–647, 2016.

[4] X. Bao and D. W. Eaton. Fault activation by hydraulic fracturing in western canada. *Science*, 354(6318):1406–1409, 2016.

[5] B. R. Barboza, B. Chen, and C. Li. A review on proppant transport modelling. *Journal of Petroleum Science and Engineering*, page 108753, 2021.

[6] M. A. Biot. General theory of three-dimensional consolidation. *Journal of applied physics*, 12 (2):155–164, 1941.

[7] T. L. Blanton et al. An experimental study of interaction between hydraulically induced and pre-existing fractures. In *SPE unconventional gas recovery symposium*. Society of Petroleum Engineers, 1982.

[8] F. Bobaru and W. Hu. The meaning, selection, and use of the peridynamic horizon and its relation to crack branching in brittle materials. *International journal of fracture*, 176(2):215–222, 2012.

[9] F. Bobaru and G. Zhang. Why do cracks branch? a peridynamic investigation of dynamic brittle fracture. *International Journal of Fracture*, 196(1-2):59–98, 2015.

[10] T. J. Boone and A. R. Ingraffea. A numerical procedure for simulation of hydraulically-driven fracture propagation in poroelastic media. *International Journal for Numerical and Analytical Methods in Geomechanics*, 14(1):27–47, 1990.

[11] B. Bourdin, C. P. Chukwudozie, K. Yoshioka, et al. A variational approach to the numerical simulation of hydraulic fracturing. In *SPE Annual Technical Conference and Exhibition*. Society of Petroleum Engineers, 2012.

[12] W. D. Callister. *Materials science and engineering an introduction*. John Wiley, 2007.

[13] T. D. Cao, E. Milanese, E. W. Remij, P. Rizzato, J. J. Remmers, L. Simoni, J. M. Huyghe, F. Hussain, and B. A. Schrefler. Interaction between crack tip advancement and fluid flow in fracturing saturated porous media. *Mechanics Research Communications*, 80:24–37, 2017.

[14] B. Carrier and S. Granet. Numerical modelling of hydraulic fracture problem in permeable medium using cohesive zone model. *Engineering fracture mechanics*, 79:312–328, 2012.

[15] B. Chen, A. R. Barron, D. Owen, and C.-F. Li. Propagation of a plane strain hydraulic fracture with a fluid lag in permeable rock. *Journal of Applied Mechanics*, 85(9), 2018.

[16] B. Chen, S. Cen, A. R. Barron, D. Owen, and C. Li. Numerical investigation of the fluid lag during hydraulic fracturing. *Engineering Computations*, 2018.

[17] B. Chen, Y. Sun, B. R. Barboza, A. R. Barron, and C. Li. Phase-field simulation of hydraulic fracturing with a revised fluid model and hybrid solver. *Engineering Fracture Mechanics*, 229: 106928, 2020.

[18] Z. Chen, J. W. Ju, G. Su, X. Huang, S. Li, and L. Zhai. Influence of micro-modulus functions on peridynamics simulation of crack propagation and branching in brittle materials. *Engineering Fracture Mechanics*, 216:106498, 2019.

[19] Z. Chen, D. Elsworth, and M. Wang. Does low-viscosity fracturing fluid always create complex fractures? *Journal of Geophysical Research: Solid Earth*, 125(9):e2020JB020332, 2020.

[20] A. Costa. Permeability-porosity relationship: A reexamination of the kozeny-carman equation based on a fractal pore-space geometry assumption. *Geophysical research letters*, 33(2), 2006.

[21] O. Coussy. *Mechanics of porous continua*. Wiley, 1995.

[22] P. A. Cundall and O. D. Strack. A discrete numerical model for granular assemblies. *geotechnique*, 29(1):47–65, 1979.

[23] B. Damjanac and P. Cundall. Application of distinct element methods to simulation of hydraulic fracturing in naturally fractured reservoirs. *Computers and Geotechnics*, 71:283–294, 2016.

[24] E. Detournay, J. McLennan, J.-C. Roegiers, et al. Poroelastic concepts explain some of the hydraulic fracturing mechanisms. In *SPE Unconventional Gas Technology Symposium*. Society of Petroleum Engineers, 1986.

[25] D. Dipasquale, G. Sarego, M. Zaccariotto, and U. Galvanetto. Dependence of crack paths on the orientation of regular 2d peridynamic grids. *Engineering Fracture Mechanics*, 160:248–263, 2016.

[26] K. Duan, C. Y. Kwok, W. Wu, and L. Jing. Dem modelling of hydraulic fracturing in permeable rock: influence of viscosity, injection rate and in situ states. *Acta Geotechnica*, 13(5):1187–1202, 2018.

[27] S. Fallahzadeh, V. Rasouli, and M. Sarmadivaleh. An investigation of hydraulic fracturing initiation and near-wellbore propagation from perforated boreholes in tight formations. *Rock Mechanics and Rock Engineering*, 48(2):573–584, 2015.

[28] S. H. Fallahzadeh, M. M. Hossain, A. James Cornwell, and V. Rasouli. Near wellbore hydraulic fracture propagation from perforations in tight rocks: the roles of fracturing fluid viscosity and injection rate. *Energies*, 10(3):359, 2017.

[29] U. Galvanetto, T. Mudric, A. Shojaei, and M. Zaccariotto. An effective way to couple fem meshes and peridynamics grids for the solution of static equilibrium problems. *Mechanics Research Communications*, 76:41–47, 2016.

[30] J. Geertsma and F. De Klerk. A rapid method of predicting width and extent of hydraulically induced fractures. *Journal of Petroleum Technology*, 21(12):1,571–1,581, 1969.

[31] J. Geertsma, F. De Klerk, et al. A rapid method of predicting width and extent of hydraulically induced fractures. *Journal of petroleum technology*, 21(12):1–571, 1969.

[32] J. Guo, Q. Lu, H. Chen, Z. Wang, X. Tang, and L. Chen. Quantitative phase field modelling of hydraulic fracture branching in heterogeneous formation under anisotropic in-situ stress. *Journal of Natural Gas Science and Engineering*, 56:455–471, 2018.

[33] T. Guo, S. Zhang, Z. Qu, T. Zhou, Y. Xiao, and J. Gao. Experimental study of hydraulic fracturing for shale by stimulated reservoir volume. *Fuel*, 128:373–380, 2014.

[34] Y. D. Ha and F. Bobaru. Studies of dynamic crack propagation and crack branching with peridynamics. *International Journal of Fracture*, 162(1-2):229–244, 2010.

[35] R. G. Jeffrey, A. Bunger, B. Lecampion, X. Zhang, Z. Chen, A. van As, D. P. Allison, W. De Beer, J. W. Dudley, E. Siebrits, et al. Measuring hydraulic fracture growth in naturally fractured rock. In *SPE annual technical conference and exhibition*. Society of Petroleum Engineers, 2009.

[36] S. Khristianovic and Y. Zheltov. Formation of vertical fractures by means of highly viscous fluids. In *Proc. 4th world petroleum congress, Rome*, volume 2, pages 579–586, 1955.

[37] B. Lecampion, A. Bunger, and X. Zhang. Numerical methods for hydraulic fracture propagation: a review of recent trends. *Journal of natural gas science and engineering*, 49:66–83, 2018.

[38] Y. Z. Ma, D. Sobernheim, and J. R. Garzon. Glossary for unconventional oil and gas resource evaluation and development. In *Unconventional Oil and Gas Resources Handbook*, pages 513–526. Elsevier, 2016.

[39] E. Madenci and E. Oterkus. Peridynamic theory. In *Peridynamic Theory and Its Applications*, pages 19–43. Springer, 2014.

[40] K. D. Mahrer. A review and perspective on far-field hydraulic fracture geometry studies. *Journal of Petroleum Science and Engineering*, 24(1):13–28, 1999.

[41] C. Miehe and S. Mauthe. Phase field modelling of fracture in multi-physics problems. part iii. crack driving forces in hydro-poro-elasticity and hydraulic fracturing of fluid-saturated porous media. *Computer Methods in Applied Mechanics and Engineering*, 304:619–655, 2016.

[42] A. Mikelic, M. F. Wheeler, and T. Wick. A phase-field method for propagating fluid-filled fractures coupled to a surrounding porous medium. *Multiscale modelling & Simulation*, 13(1): 367–398, 2015.

[43] A. Mikelić, M. F. Wheeler, and T. Wick. A quasi-static phase-field approach to pressurized fractures. *Nonlinearity*, 28(5):1371, 2015.

[44] T. Mohammadnejad and A. Khoei. An extended finite element method for hydraulic fracture propagation in deformable porous media with the cohesive crack model. *Finite Elements in Analysis and Design*, 73:77–95, 2013.

[45] S. Nadimi, I. Miscovic, and J. McLennan. A 3d peridynamic simulation of hydraulic fracture process in a heterogeneous medium. *Journal of Petroleum Science and Engineering*, 145:444–452, 2016.

[46] M. J. Nasehi and A. Mortazavi. Effects of in-situ stress regime and intact rock strength parameters on the hydraulic fracturing. *Journal of Petroleum Science and Engineering*, 108:211–221, 2013.

[47] N. M. Newmark. A method of computation for structural dynamics. *Journal of the engineering mechanics division*, 85(3):67–94, 1959.

[48] V. P. Nguyen, H. Lian, T. Rabczuk, and S. Bordas. Modelling hydraulic fractures in porous media using flow cohesive interface elements. *Engineering Geology*, 225:68–82, 2017.

[49] L. Ni, X. Zhang, L. Zou, and J. Huang. Phase-field modelling of hydraulic fracture network propagation in poroelastic rocks. *Computational Geosciences*, pages 1–16, 2020.

[50] T. Ni, Q.-z. Zhu, L.-Y. Zhao, and P.-F. Li. Peridynamic simulation of fracture in quasi brittle solids using irregular finite element mesh. *Engineering Fracture Mechanics*, 188:320–343, 2018.

[51] T. Ni, M. Zaccariotto, Q.-Z. Zhu, and U. Galvanetto. Static solution of crack propagation problems in peridynamics. *Computer Methods in Applied Mechanics and Engineering*, 346:126–151, 2019.

[52] T. Ni, F. Pesavento, M. Zaccariotto, U. Galvanetto, Q.-Z. Zhu, and B. A. Schrefler. Hybrid fem and peridynamic simulation of hydraulic fracture propagation in saturated porous media. *Computer Methods in Applied Mechanics and Engineering*, 366:113101, 2020.

[53] T. Ni, F. Pesavento, M. Zaccariotto, U. Galvanetto, and B. A. Schrefler. Numerical simulation of forerunning fracture in saturated porous solids with hybrid fem/peridynamic model. *Computers and Geotechnics*, 133:104024, 2021.

[54] S. Oterkus, E. Madenci, and E. Oterkus. Fully coupled poroelastic peridynamic formulation for fluid-filled fractures. *Engineering geology*, 225:19–28, 2017.

[55] H. Ouchi, A. Katiyar, J. York, J. T. Foster, and M. M. Sharma. A fully coupled porous flow and geomechanics model for fluid driven cracks: a peridynamics approach. *Computational Mechanics*, 55(3):561–576, 2015.

[56] S. Rahimi-Aghdam, V.-T. Chau, H. Lee, H. Nguyen, W. Li, S. Karra, E. Rougier, H. Viswanathan, G. Srinivasan, and Z. P. Bažant. Branching of hydraulic cracks enabling permeability of gas or oil shale with closed natural fractures. *Proceedings of the National Academy of Sciences*, 116(5):1532–1537, 2019.

[57] K. Ravi-Chandar and W. Knauss. An experimental investigation into dynamic fracture: Ii. microstructural aspects. *International Journal of Fracture*, 26(1):65–80, 1984.

[58] K. Ravi-Chandar and W. Knauss. An experimental investigation into dynamic fracture: Iii. on steady-state crack propagation and crack branching. *International Journal of Fracture*, 26(2): 141–154, 1984.

[59] Q. Ren, Y. Dong, and T. Yu. Numerical modelling of concrete hydraulic fracturing with extended finite element method. *Science in China Series E: Technological Sciences*, 52(3):559–565, 2009.

[60] J. R. Rice and M. P. Cleary. Some basic stress diffusion solutions for fluid-saturated elastic porous media with compressible constituents. *Reviews of Geophysics*, 14(2):227–241, 1976.

[61] D. Santillán, R. Juanes, and L. Cueto-Felgueroso. Phase field model of hydraulic fracturing in poroelastic media: Fracture propagation, arrest, and branching under fluid injection and extraction. *Journal of Geophysical Research: Solid Earth*, 123(3):2127–2155, 2018.

[62] E. Sarris and P. Papanastasiou. The influence of the cohesive process zone in hydraulic fracturing modelling. *International Journal of Fracture*, 167(1):33–45, 2011.

[63] A. Savitski and E. Detournay. Propagation of a penny-shaped fluid-driven fracture in an impermeable rock: asymptotic solutions. *International journal of solids and structures*, 39(26): 6311–6337, 2002.

[64] S. Secchi and B. Schrefler. A method for 3-d hydraulic fracturing simulation. *International journal of fracture*, 178(1-2):245–258, 2012.

[65] H. Shimizu, S. Murata, and T. Ishida. The distinct element analysis for hydraulic fracturing in hard rock considering fluid viscosity and particle size distribution. *International Journal of Rock Mechanics and Mining Sciences*, 48(5):712–727, 2011.

[66] S. A. Silling. Reformulation of elasticity theory for discontinuities and long-range forces. *Journal of the Mechanics and Physics of Solids*, 48(1):175–209, 2000.

[67] S. A. Silling and E. Askari. A meshfree method based on the peridynamic model of solid mechanics. *Computers & structures*, 83(17-18):1526–1535, 2005.

[68] S. A. Silling, M. Epton, O. Weckner, J. Xu, and E. Askari. Peridynamic states and constitutive modeling. *Journal of Elasticity*, 88(2):151–184, 2007.

[69] D. Spence and P. Sharp. Self-similar solutions for elastohydrodynamic cavity flow. *Proceedings of the Royal Society of London. A. Mathematical and Physical Sciences*, 400(1819):289–313, 1985.

[70] K. Terzaghi. *Theoretical Soil Mechanics*. John Wiley Sons, 1943.

[71] D. Tiab and E. C. Donaldson. *Petrophysics: theory and practice of measuring reservoir rock and fluid transport properties*. Gulf professional publishing, 2015.

[72] D. Z. Turner. A non-local model for fluid-structure interaction with applications in hydraulic fracturing. *International Journal for Computational Methods in Engineering Science and Mechanics*, 14(5):391–400, 2013.

[73] H. F. Wang. *Theory of linear poroelasticity with applications to geomechanics and hydrogeology*, volume 2. Princeton University Press, 2000.

[74] H. Xu, W. Zhou, R. Xie, L. Da, C. Xiao, Y. Shan, and H. Zhang. Characterization of rock mechanical properties using lab tests and numerical interpretation model of well logs. *Mathematical Problems in Engineering*, 2016, 2016.

[75] Z. Yushi, Z. Shicheng, Z. Tong, Z. Xiang, and G. Tiankui. Experimental investigation into hydraulic fracture network propagation in gas shales using ct scanning technology. *Rock Mechanics and Rock Engineering*, 49(1):33–45, 2016.

[76] M. Zaccariotto, T. Mudric, D. Tomasi, A. Shojaei, and U. Galvanetto. Coupling of fem meshes with peridynamic grids. *Computer Methods in Applied Mechanics and Engineering*, 330:471–497, 2018.

[77] B. Zhang, X. Li, Z. Zhang, Y. Wu, Y. Wu, and Y. Wang. Numerical investigation of influence of in-situ stress ratio, injection rate and fluid viscosity on hydraulic fracture propagation using a distinct element approach. *Energies*, 9(3):140, 2016.

[78] F. Zhang, E. Dontsov, and M. Mack. Fully coupled simulation of a hydraulic fracture interacting with natural fractures with a hybrid discrete-continuum method. *International Journal for Numerical and Analytical Methods in Geomechanics*, 41(13):1430–1452, 2017.

[79] Q. Zhang, X.-P. Zhang, and W. Sun. Hydraulic fracturing in transversely isotropic tight sandstone reservoirs: A numerical study based on bonded-particle model approach. *Journal of Structural Geology*, page 104068, 2020.

[80] S. Zhou, X. Zhuang, and T. Rabczuk. Phase-field modeling of fluid-driven dynamic cracking in porous media. *Computer Methods in Applied Mechanics and Engineering*, 350:169–198, 2019.

[81] O. Zienkiewicz and A. Chan. Coupled problems and their numerical solution. In *Advances in Computational Nonlinear Mechanics*, pages 139–176. Springer, 1989.